

# Validation of NeQuick topside ionospheric formulation using selected COSMIC/FORMOSAT-3 data and possible improvements

Singh Arun Kumar<sup>1</sup>, Haralambous Haris<sup>2</sup>, and Oikonomou Christina<sup>3</sup>

<sup>1</sup>Frederick Research Center

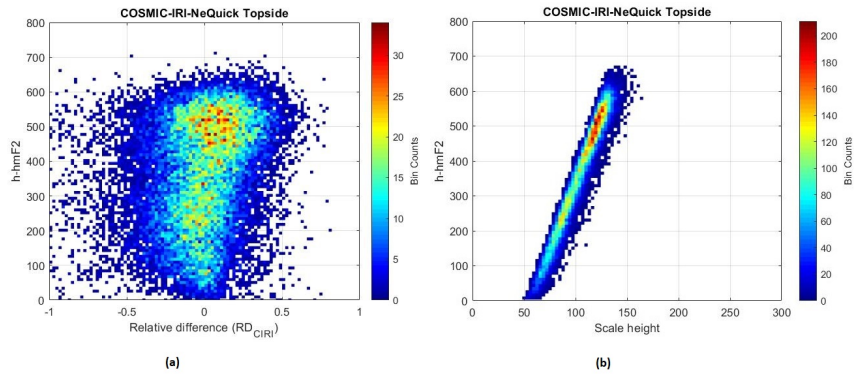
<sup>2</sup>Frederick University

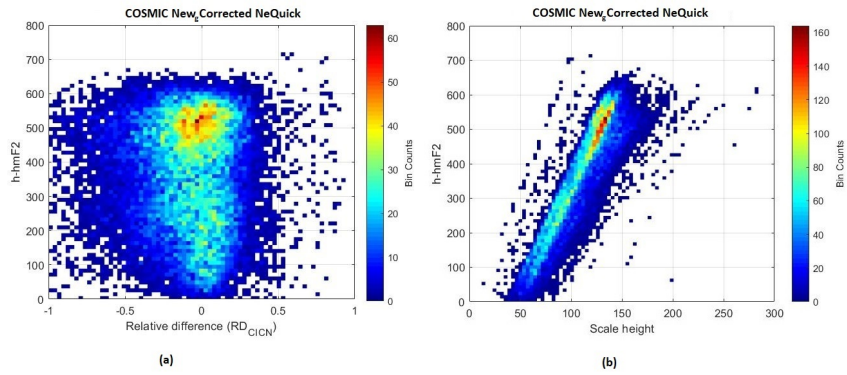
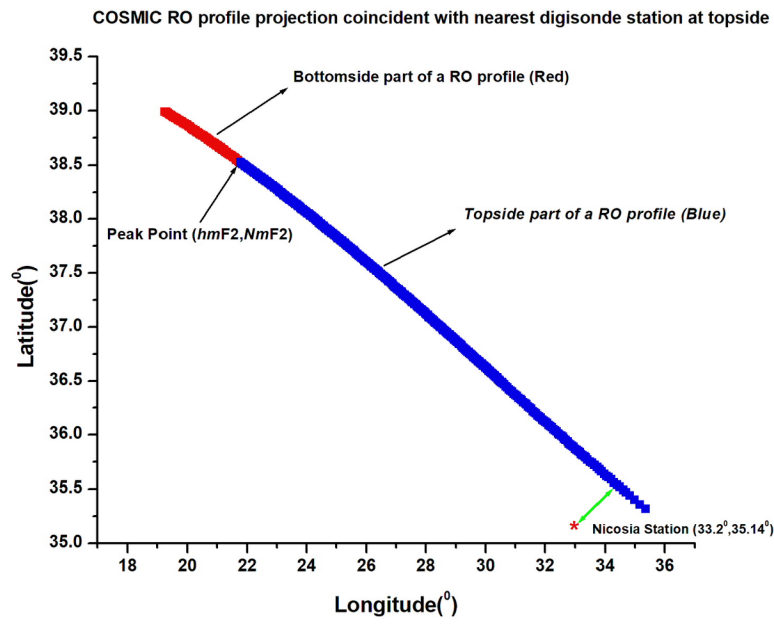
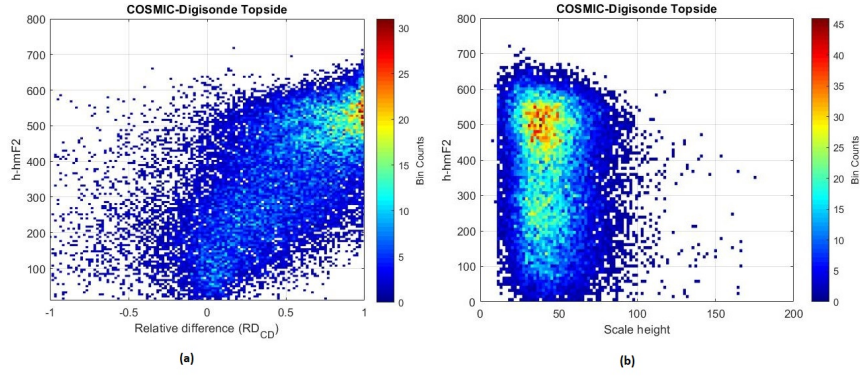
<sup>3</sup>Frederick Research Center, Nicosia

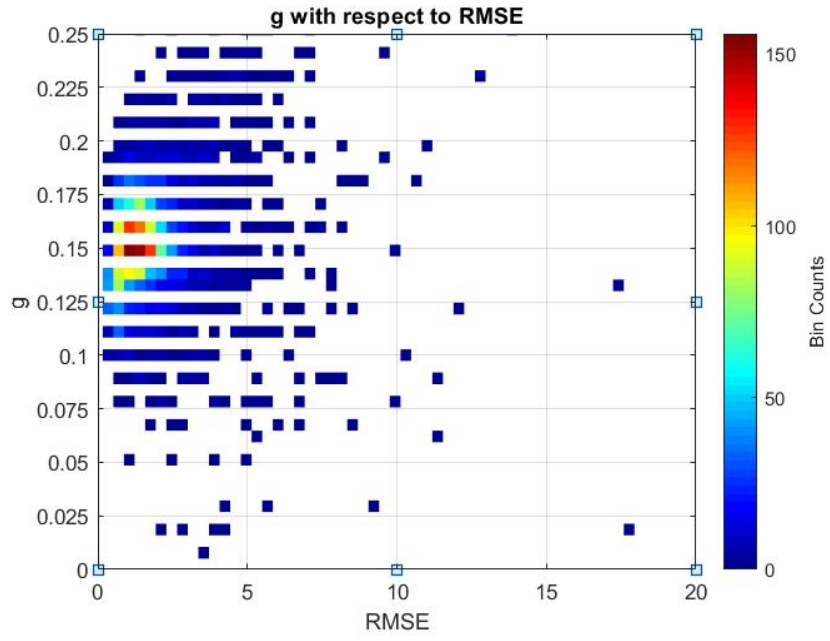
November 15, 2022

## Abstract

We examine systematic differences between topside electron density measurements and different topside model formulations including ground-based  $\alpha$ -Chapman extrapolated topside electron density profiles from auto scaled ionograms, International Reference Ionosphere Model (IRI-2016) NeQuick topside estimations and a recently improved NeQuick (Corrected NeQuick) topside formulation. The selected topside electron density measurements considered were taken, from radio occultation electron density profiles on board low Earth orbit (LEO) satellites from the COSMIC/FORMOSAT-3 mission, in the vicinity of digisonde stations on a global scale. A subset of these radio occultation profiles, with matched (within 5%) peak NmF2 and hmF2 characteristics is also exploited to focus the comparison to a high quality validation dataset. The comparison shows that  $\alpha$ -Chapman and Corrected NeQuick underestimate, whereas IRI-NeQuick overestimates COSMIC topside electron density observations. The key parameter  $g$  which controls the change of scale height w.r.t. altitude near the F region peak is optimised to a value of 0.15 (compared to a currently adopted value of 0.125). The Corrected NeQuick topside formulation using the optimised  $g$  value of 0.15 (represented as  $New_g$ ) outperforms all other topside formulations.







1           **Validation of NeQuick topside ionospheric formulation using selected**  
2           **COSMIC/FORMOSAT-3 data and possible improvements**

3           Arun Kumar Singh<sup>2</sup>, Haris Haralambous<sup>1,2</sup>, Christina Oikonomou<sup>2</sup>

4  
5           1. Department of Electrical Engineering, Frederick University, Nicosia, Cyprus

6  
7           2. Frederick Research Center 7 Filokyprou Street, Pallouriotissa 1036, Nicosia, Cyprus

8  
9           Corresponding author Email: [arsurya123@gmail.com](mailto:arsurya123@gmail.com)

10  
11          **Key Points:**

- 12
- 13          •  $\alpha$ -Chapman and Corrected NeQuick underestimate, whereas IRI-NeQuick
  - 14            overestimates COSMIC topside electron density measurements.
  - 15          • Corrected NeQuick provides a better topside representation among all three topside
  - 16            formulations.
  - 17          • Corrected NeQuick topside formulation further improves with an optimised value of  $g$
  - 18            = 0.15.
- 19  
20  
21  
22  
23  
24  
25  
26  
27  
28  
29  
30  
31  
32  
33  
34

35

## 36 **Abstract**

37 We examine systematic differences between topside electron density measurements and  
38 different topside model formulations including ground-based  $\alpha$ -Chapman extrapolated  
39 topside electron density profiles from auto scaled ionograms, International Reference  
40 Ionosphere Model (IRI-2016) NeQuick topside estimations and a recently improved NeQuick  
41 (Corrected NeQuick) topside formulation. The selected topside electron density  
42 measurements considered were taken, from radio occultation electron density profiles on  
43 board low Earth orbit (LEO) satellites from the COSMIC/FORMOSAT-3 mission, in the  
44 vicinity of digisonde stations on a global scale. A subset of these radio occultation profiles,  
45 with matched (within 5%) peak NmF2 and hmF2 characteristics is also exploited to focus the  
46 comparison to a high quality validation dataset. The comparison shows that  $\alpha$ -Chapman and  
47 Corrected NeQuick underestimate, whereas IRI-NeQuick overestimates COSMIC topside  
48 electron density observations. The key parameter  $g$  which controls the change of scale height  
49 w.r.t. altitude near the F region peak is optimised to a value of 0.15 (compared to a currently  
50 adopted value of 0.125). The Corrected NeQuick topside formulation using the optimised  $g$   
51 value of 0.15 (represented as New<sub>g</sub>) outperforms all other topside formulations.

## 52 **1. Introduction**

53 The COSMIC/FORMOSAT-3 (Constellation Observing System for Meteorology,  
54 Ionosphere, and Climate and Formosa Satellite) mission has been very successful in  
55 facilitating the vertical profiling of the atmosphere and the study of the topside ionosphere  
56 (Anthes R.A. et al., 2008). The radio occultation (RO) technique is based on precise dual-  
57 frequency phase measurements (Schreiner et al., 1999) from GNSS receivers on board Low-  
58 Earth Orbit (LEO) satellites that exploit radio signals transmitted from global navigation  
59 satellite system (GNSS) satellites. Many authors have worked on the validation of COSMIC  
60 data using co-located digisonde and Incoherent Scatter Radar (ISR) stations (Stankov and  
61 Jakowski, 2006; Lei et al., 2007; Krankowski et al., 2011; Yue et al., 2011; Cherniak and  
62 Zakharenkova, 2014; Hu et al., 2014; McNamara and Thompson, 2015; Panda et al., 2018;  
63 Shaikh et al., 2018; Wang et al., 2019; Bai et al., 2019).

64 The topside part of the ionosphere is defined as the region between the maximum electron  
65 density of the F2 layer to the upper transition height (Rishbeth and Garriott, 1969). The  
66 transition of heavy O<sup>+</sup> ions to lighter H<sup>+</sup> ions leads to a smooth decrease in the electron

67 density. This smooth decrease is expressed by a parameter called scale height (Hargreaves,  
68 1992). To determine the scale height, the information of the mean ion mass, their chemical  
69 state and plasma temperature must be known but this information is not available on a global  
70 scale. So there are alternative methods to estimate the effective scale height based on electron  
71 density measurements (Liu et al., 2007a, 2007b) since to accurately model the topside  
72 ionosphere, the effective scale height is a major requirement.

73 The International Ionosphere Model (IRI) -2016 (Bilitiza et al., 2017) offers three options to  
74 model the electron density in the topside ionosphere, IRI-2001 (Bilitiza, 1990), IRI01-corr  
75 (Bilitiza, 2004) and the most reliable NeQuick (Radicella and Leitinger, 2001; Coisson et al.,  
76 2006; Nava et al., 2008) but according to past and recent studies there is still room for  
77 improvement (Bilitiza et al., 2006, Bilitiza, 2009; Pignalberi et al., 2016). The NeQuick  
78 topside model uses an Epstein function (as shown in equation 1) to model the topside  
79 ionosphere. The electron density profile (Ne (h)) is constructed as a function of  $hmF2$ ,  $NmF2$   
80 and effective scale height (Hm).

$$81 \quad Ne(h) = 4.NmF2 \cdot \frac{\exp\left(\frac{h-hmF2}{Hm}\right)}{\left(1+\exp\left(\frac{h-hmF2}{Hm}\right)\right)^2} \quad (1)$$

$$82 \quad Hm = H_0 \left[ 1 + \frac{r \cdot g(h-hmF2)}{r \cdot H_0 + g \cdot (h-hmF2)} \right] \quad (2)$$

83 The scale height in the NeQuick topside formulation is described by three parameters, scale  
84 height at the peak ( $H_0$ ), parameter  $r$  which restricts the scale height at higher altitudes and the  
85 altitude gradient of the scale height ( $g$ ). A value of  $r = 100$  and  $g = 0.125$  is adopted in  
86 NeQuick topside formulation, while  $H_0$  is estimated from equation (3), where  $f_oF2$  is the peak  
87 critical frequency,  $NmF2$  is the peak electron density,  $hmF2$  is the height corresponding to  
88  $NmF2$  and  $R12$  is the 12 month smoothed sunspot number.

$$89 \quad H_0 = k \cdot B2_{Bot} \quad (3)$$

$$90 \quad k = 3.22 - 0.0538 \cdot f_oF2 - 0.00664 \cdot hmF2 + 0.113 \cdot \frac{hmF2}{B2_{Bot}} + 0.00257 \cdot R12 \quad (4)$$

91 An improvement in the NeQuick topside formulation (NeQuick-corr [Pezzopane and  
92 Pignalberi, 2019]) has been recently proposed. This Corrected NeQuick topside formulation  
93 is based on  $H_0$  grids, as a function of  $hmF2$  and  $NmF2$ , generated by applying the IRI-UP  
94 (Update) method (Pignalberi et al., 2018) and also by exploiting electron density values  
95 measured by the Langmuir probes on-board Swarm satellites. According to this method,  $H_0$  is

96 estimated as  $H_{0, AC}$  and  $H_{0, B}$  at two different altitudes for each pair of  $hmF2$  and  $NmF2$  values  
97 to determine a new  $H_0$  formulation in accordance to equations (45) and (6).

$$98 \quad H_0 = H_{0, AC} + (H_{0, B} - H_{0, AC}) \cdot \frac{h - hmF2}{600} \quad \text{for } hmF2 \leq h < hmF2 + 600 \quad (5)$$

$$99 \quad H_0 = H_{0, B} \quad \text{for } h \geq hmF2 + 600 \quad (6)$$

100 where two 2-D grids provide the values of  $H_{0, AC}$  and  $H_{0, B}$  as a function of  $foF2$  and  $hmF2$ .

101 Themens et al., 2018 demonstrated that the IRI-NeQuick option can be improved over upper  
102 mid latitude and high latitude regions by adjusting  $r$  and  $g$  values to  $r = 20$  and  $g = 0.2024$ .  
103 Another study by Themens et al., 2014 showed that IRI-NeQuick parameterization does not  
104 adequately represent the topside thickness during solar minimum between cycles 23 and 24  
105 and Pignalberi et al., 2020 underlined the significance of  $r$  and  $g$  in the topside scale height  
106 variation near the F2-layer peak (up to about 800 km). They have shown that the topside  
107 scale height exhibits a linear dependence on the peak-relative altitude ( $h - hmF2$ ), where  $g$  is  
108 the slope and  $H_0$  is the intercept, as follows:

$$109 \quad H(h) \simeq H_0 + g \times (h - hmF2) \quad (7)$$

110 In view of the above, in this paper, topside electron density values retrieved from 29063  
111 COSMIC RO profiles in the vicinity of 44 digisonde stations are compared with  $\alpha$ -Chapman,  
112 IRI-NeQuick, and Corrected-NeQuick topside model electron density estimates. Furthermore,  
113 we show that a new  $g$  value of 0.15 produces better results using Corrected-NeQuick. To  
114 validate this new  $g$  value in the Corrected-NeQuick topside formulation, scale height has  
115 been deduced from each COSMIC RO based on the valid assumption (up to 800 km) of a  
116 linear dependence with altitude. This could be significant, in the context of the single-  
117 frequency GNSS correction algorithm (NeQuick-G) adopted by European Space Agency  
118 (ESA) Galileo GNSS system, as  $r = 100$  and  $g = 0.125$  are the values embedded in the existing  
119 version of NeQuick-G.

## 120 **2. Data**

121 The comparison between topside COSMIC RO profiles (downloaded from the CDAAC data  
122 server <https://cdaac-www.cosmic.ucar.edu/cdaac/products.html>) and digisonde topside  
123 profiles was carried out under time and space coincidence requirements. In particular the  
124 COSMIC topside electron density value considered, was the one at a minimum distance to  
125 the digisonde location (as shown in Figure 1). Figure 1 shows the COSMIC RO profile with  
126 respect to latitude and longitude, where the red part of the profile shows the bottomside

127 projection and blue part shows the topside profile projection. It also shows the nearest  
 128 digisonde station (Nicosia station as an example) and the minimum (perpendicular) distance  
 129 between digisonde station and topside profile. We have also excluded any unrealistic RO  
 130 profiles with excessive fluctuations in the topside electron density and hmF2 outside the  
 131 range [150<hmF2<450] km. In total 29063 profiles in the interval 2006-2018 were  
 132 considered. The autoscaled digisonde data were downloaded from the Digital Ionogram Data  
 133 Base (DIDBase- <http://giro.uml.edu/didbase/scaled.php>). The selected digisonde stations,  
 134 their location (latitude, longitude) and the number of nearest selected COSMIC profiles are  
 135 shown in Table 1. To construct the digisonde topside electron density profile, *hmF2*, *foF2* and  
 136 scale height values were applied in  $\alpha$ -Chapman function, shown in equation (8):

$$137 \quad N_e(h) = NmF2 \cdot \exp \left\{ \frac{1}{2} \left[ 1 - \frac{h-hmF2}{H} \exp \left( -\frac{h-hmF2}{H} \right) \right] \right\} \quad (8)$$

138 The corresponding IRI-NeQuick values were also estimated at the corresponding COSMIC  
 139 topside electron density altitude (at a minimum distance from the corresponding digisonde)  
 140 using the FORTRAN source code for IRI 2016, available at <http://irimodel.org/> by ingesting  
 141 *hmF2* and *foF2* auto-scaled values. The Corrected-NeQuick values were estimated by  
 142 calculating  $H_0$  using the  $H_{0,AC}$  and  $H_{0,B}$  grid (downloaded from the supplementary data of the  
 143 Pezzopane and Pignalberi, (2019)) for the same *hmF2* and *NmF2* values. This dataset is  
 144 termed as DATABASE 1. To compare COSMIC to  $\alpha$ -Chapman (digisonde), IRI-NeQuick,  
 145 Corrected NeQuick and New<sub>g</sub> Corrected NeQuick data, relative differences were calculated  
 146 as shown below:

$$147 \quad \text{Relative difference (RD}_{CD}) = \frac{\text{COSMIC electron density} - \text{digisonde electron density}}{\text{COSMIC electron density}} \quad (9)$$

$$149 \quad \text{Relative difference (RD}_{CIRI}) = \frac{\text{COSMIC electron density} - \text{IRI-NeQuick model electron density}}{\text{COSMIC electron density}} \quad (10)$$

$$151 \quad \text{Relative difference (RD}_{CCN}) = \frac{\text{COSMIC electron density} - \text{Corrected NeQuick model electron density}}{\text{COSMIC electron density}} \quad (11)$$

$$153 \quad \text{Relative difference (RD}_{CICN}) = \frac{\text{COSMIC electron density} - \text{New}_g \text{Corrected NeQuick model electron density}}{\text{COSMIC electron density}}$$

154

155 (12)

156 The second dataset used in this investigation is based on a subset of DATASET 1 for which  
157 coincidence at the peak values ( $NmF2$ ,  $hmF2$ ) of the profile within <5% difference in  $hmF2$   
158 and  $NmF2$  was satisfied, in an effort to ensure more reliable topside profiles in accordance to  
159 findings in a previous study (Shaikh et al., 2018). We have found thirty four hundred thirty  
160 three (3433) such cases out of 29,063 cases from DATASET 1, based on which, we have  
161 calculated corresponding IRI-NeQuick, Corrected NeQuick and New<sub>g</sub> Corrected profiles.  
162 This dataset is termed as DATASET 2.

163 To compare the full topside profiles recorded by the COSMIC RO satellites and modeled by  
164  $\alpha$ -Chapman (digisonde), IRI-NeQuick, Corrected NeQuick and New<sub>g</sub> Corrected NeQuick a  
165 relative difference (as a function of altitude beyond the peak) was calculated as shown below:

$$166 \text{ Relative difference (RD}_{CD}(h)) = \frac{\text{COSMIC electron density (h)} - \text{digisonde electron density(h)}}{\text{COSMIC electron density (h)}}$$

167 (13)

$$168 \text{ Relative difference (RD}_{CIRI}(h)) = \frac{\text{COSMIC electron density (h)} - \text{IRI-NeQuick model electron density(h)}}{\text{COSMIC electron density (h)}}$$

169 (14)

$$170 \text{ Relative difference (RD}_{CCN}(h)) = \frac{\text{COSMIC electron density(h)} - \text{Corrected NeQuick electron density(h)}}{\text{COSMIC electron density(h)}}$$

171 (15)

$$172 \text{ Relative difference (RD}_{CICN}(h)) = \frac{\text{COSMIC electron density (h)} - \text{New}_g\text{Corrected NeQuick model electron density (h)}}{\text{COSMIC electron density (h)}}$$

174 (16)

175 and,

$$176 \quad \quad \quad h_{top} = h - hmF2 \quad \quad \quad (17)$$

177  $h_{top}$  denotes the peak-relative altitude in km.

178 To investigate the overall performance in terms of the full profile in the various topside  
179 formulations, a Normalised Root Mean Square Error (NRMSE) was calculated for each of the  
180 3433 profiles for DATASET 2, using:

$$181 \quad \text{NRMSE} = \sqrt{\frac{\sum_{i=1}^N \left( \frac{N_{e_{measured},i} - N_{e_{modeled},i}}{N_{e_{measured},i}} \right)^2}{N}} \quad (18)$$

182 where subscript *measured* refers to COSMIC measurements, while *modeled* to either  $\alpha$ -  
183 Chapman, IRI-NeQuick or Corrected NeQuick.  $N$  is the total number of electron density  
184 profile points.

185 The scale height (Hm) was calculated for COSMIC,  $\alpha$ -Chapman, IRI-NeQuick and Corrected  
186 NeQuick data from the Epstein equation as shown below. Pignalberi et al., (2020) also have  
187 used same approach to calculate scale height from COSMIC profile.

$$188 \quad N(h) = 4 \cdot NmF2 \cdot \frac{\exp\left(\frac{h-hmF2}{Hm}\right)}{\left(1 + \exp\left(\frac{h-hmF2}{Hm}\right)\right)^2} \quad (19)$$

$$\frac{N(h)}{4NmF2} = \frac{\exp\left(\frac{h-hmF2}{Hm}\right)}{\left(1 + \exp\left(\frac{h-hmF2}{Hm}\right)\right)^2}$$

189 Let,

$$190 \quad Y = \exp\left(\frac{h-hmF2}{Hm}\right) \quad (20)$$

$$191 \quad X = \frac{N(h)}{4NmF2} \quad (21)$$

192 then the equation becomes:

$$193 \quad X(1+Y)^2 = Y$$

$$194 \quad X Y^2 + (2X-1) Y + X = 0 \quad (22)$$

195 By using the Sridhar Acharya formula, the solution for the above quadratic equation reduces  
196 to:

$$197 \quad Y(1, 2) = \frac{[(2NmF2 - N(h)) \pm 2\sqrt{NmF2^2 - N(h) \cdot NmF2}]}{N(h)} \quad (23)$$

198 and by solving equation (19) and (23), Hm would be:

$$199 \quad Hm = \frac{h-hmF2}{\ln Y(1,2)} \quad (24)$$

200 The calculated scale height from equation 24 was used to check the linear fit dependence.

201        **3. Results:**

202        The comparison between topside electron density profile measurements and model  
203        formulations, as described in section 2 is presented in the following sections. The results in  
204        section (3.1) are based on DATASET 1 and section (3.2) and (3.3) are based on DATASET  
205        2.

206        **3.1 Comparison based on DATASET 1**

207        Figure 2 (a) shows the binned scatter plot between peak-relative altitude ( $h_{top}=h-hmF2$ ) and  
208        relative difference ( $RD_{CD}$ ) between COSMIC observations and  $\alpha$ -Chapman estimations,  
209        while the colour bar shows the counts in each bin. As it can be seen from the graph, in the  
210        vast majority of cases  $RD_{CD}$  is greater than zero which indicates that  $\alpha$ -Chapman  
211        underestimates COSMIC observations and this difference increases with  $h_{top}$  with the bin  
212        occurrence maximising around 500 km (above  $hmF2$ ). The findings from Figure 2 (a) are  
213        justified because digisonde topside estimation is based on a  $\alpha$ -Chapman function, with a  
214        constant scale height (as shown in Figure 2 (b)), but real observations differ from  $\alpha$ -Chapman  
215        estimates because scale height increases linearly with height over the peak (Olivares-Pulido  
216        et al., 2016). The scale height behaviour of COSMIC observations (as shown in Figure 5) was  
217        calculated from DATASET 1 using equation 24.

218        Figure 3(a) shows the binned scatter plot between peak-relative altitude ( $h_{top}$ ) and relative  
219        difference ( $RD_{CIRI}$ ) between COSMIC observations and IRI-NeQuick estimates. It shows that  
220        IRI-NeQuick slightly overestimates the COSMIC observations up to an approximate  $h_{top}$   
221        altitude of 300km and then its behaviour reverses underestimating COSMIC measurements.  
222        IRI-NeQuick is based on an Epstein function to represent the topside profile with an  
223        approximately linear scale height (calculated using equation 24, as shown in Figure 3 (b)) and  
224        therefore its performance is superior to  $\alpha$ -Chapman. The IRI-NeQuick considers values of  
225         $r=100$  and  $g=0.125$  for calculating the scale height. The error with respect to  $h_{top}$  as shown in  
226        Figure 3 (a) could be due to the difference in the change of scale height with w.r.t.  $h_{top}$  (g)  
227        between COSMIC observations and IRI-NeQuick estimations (Themens et al., 2018).

228        Figure 4 (a) shows the binned scatter plot between peak-relative altitude ( $h_{top}$ ) and relative  
229        difference ( $RD_{CCN}$ ) between COSMIC observations and Corrected NeQuick estimates. It  
230        shows that Corrected NeQuick underestimates COSMIC observations and this  
231        underestimation increases with  $h_{top}$ . The Corrected NeQuick is equivalent to IRI-NeQuick  
232        but the value of  $H_0$  is deduced from  $H_{0,AC}$  and  $H_{0,B}$  grids and the scale height (as shown in

233 Figure 4 (b)) is calculated by equation 24 following equations 5 and 6 as proposed by  
234 Pezzopane and Pignalberi, (2019). As it is clear from Figure 3 (a) and Figure 4 (a), for the  
235 majority of cases IRI-NeQuick exhibits an approximate error in the range -0.2 to 0.4 and for  
236 Corrected NeQuick the error lies in the range of 0 to 0.35 respectively, which demonstrates  
237 that Corrected NeQuick outperforms IRI-NeQuick.

238 The above results clearly indicate that the scale height calculated using different  $H_0$   
239 formulations is not able to match the scale height calculated from COSMIC observations and  
240 that further potential improvement could be achieved by more appropriate values for  $r$  and  $g$   
241 (Themens et al., 2018). To explore this possibility, we used least squares to optimize the  
242 value of  $g$  and  $r$  keeping  $H_0$  constant for Corrected NeQuick. The value of  $r$  varied with a step  
243 size of 1 and  $g$  with a step size of 0.01. As the COSMIC data were mostly limited to an  
244 altitude below 800 km, since  $r$  controls the scale height at higher altitudes,  $r$  did not change  
245 at all during this optimization ( $r=100$ ). Pignalberi et al., (2020) also showed that the effect of  
246 varying  $r$  on the scale height, is seen on the altitude much higher from the F2 peak. Figure 6  
247 shows the variation of  $r$  and  $g$  with respect to the RMSE calculated between COSMIC  
248 observations and Corrected-NeQuick estimates. COSMIC and Corrected NeQuick  
249 comparison showed that for  $r=100$  and an optimised value of  $g=0.15$ , RMSE minimizes. In  
250 this method, to estimate the electron density, the Epstein equation was used and scale height  
251 was calculated using  $H_0$  extracted from the  $H_{0,AC}$  and  $H_{0,B}$  grid  $r=100$  and  $g=0.15$ . Figure 7  
252 (a) shows the binned scatter plot between peak-relative altitude and relative difference  
253 ( $RD_{CICN}$ ) between COSMIC observations and  $New_g$  Corrected NeQuick estimates. It shows  
254 that the  $RD_{CICN}$  is almost constant with  $h_{top}$  and it is confined within a bounded region. So  
255 by comparing all four methods (Figure 2, 3, 4&7) it can be stated that the performance of  
256  $New_g$  Corrected NeQuick method is better than the other four methods for this particular  
257 dataset. The scale height (calculated from equation 24 for  $New_g$  Corrected NeQuick method  
258 is shown in Figure 7 (b).

### 259 **3.2 Comparison based on DATASET 2**

260 DATASET 2 is a subset of DATASET 1 comprising of 3433 matched peak profiles (within  
261 <5% difference in  $hmF2$  and  $NmF2$ ). Figure 8 (a) and (b) show the binned scatter plot  
262 between peak-relative altitude ( $h_{top}=h-hmF2$ ) and relative difference ( $RD_{CD}(h)$ ) between  
263 COSMIC and  $\alpha$ -Chapman profiles, for  $h-hmF2>100$  and  $h-hmF2<100$  respectively. The  
264 colour bar represents the counts in each bin. As discussed in section (3.1),  $\alpha$ -Chapman

265 underestimates COSMIC observations and it increases with  $h_{top}$ , which can also be observed  
266 from Figure 8(a) as  $RD_{CD}(h)$  increases with  $h_{top}$ . Figure 8 (b) shows that up to 100 km over  
267  $hmF2$ , the average  $RD_{CD}(h)$  fluctuates around zero. This is expected as  $\alpha$ -Chapman scale  
268 height is constant, around the peak.

269 Figure 9 (a) and (b) show scatter plots between peak-relative altitude ( $h_{top}$ ) and relative  
270 difference ( $RD_{CIRI}(h)$ ) between COSMIC profile and IRI-NeQuick estimated profile, for  $h$ -  
271  $hmF2 > 100$  and  $h$ - $hmF2 < 100$  respectively. Figure 9 (a) shows that IRI-NeQuick overestimates  
272 (-0.5 to 0 for the majority of profiles) COSMIC up to approximately  $h_{top} = 300$  km and then its  
273 behaviour reverses with a definite underestimation (within 0 to 0.2 for most profiles). The  
274 results are similar with the findings discussed in section (3.1) indicating that IRI-NeQuick  
275 clearly outperforms  $\alpha$ -Chapman. Figure 9 (b) shows that up to  $h_{top} = 100$  km, the average  
276  $RD_{CIRI}(h)$  fluctuates around 0, which suggests that IRI-NeQuick also exhibits approximately  
277 constant scale height around the peak.

278 Figure 10 (a) and (b) shows the binned scatter plot between peak-relative altitude ( $h_{top}$ ) and  
279 relative difference ( $RD_{CCN}(h)$ ) between COSMIC and Corrected NeQuick, for  $h$ - $hmF2 > 100$   
280 km and  $h$ - $hmF2 < 100$  km respectively. Figure 10 (a) shows that Corrected NeQuick  
281 underestimates COSMIC and  $RD_{CCN}(h)$  increases (0 to 0.5) with  $h_{top}$ . Unlike IRI-NeQuick,  
282 the behaviour of Corrected NeQuick does not reverse with  $h_{top}$ , whereas the  $RD_{CCN}(h)$  gets  
283 saturated for  $h_{top} > 300$  km. Figure 10 (b) shows that up to  $h_{top} = 100$  km average  $RD_{CCN}(h)$   
284 fluctuates around zero suggesting that like  $\alpha$ -Chapman and IRI-NeQuick, Corrected NeQuick  
285 also exhibits nearly constant scale height around the peak.

286 NRMSE between COSMIC and the three topside formulations was also calculated. Figure 11  
287 (a) shows the scatter plot between the NRMSE values for Corrected NeQuick (w.r.t.  
288 COSMIC) on x axis and NRMSE values for  $\alpha$ -Chapman (w.r.t. COSMIC) on y axis. For the  
289 majority of cases NRMSE- $\alpha$ -Chapman exceeds NRMSE-Corrected NeQuick, which means  
290 Corrected NeQuick performs better than  $\alpha$ -Chapman. Figure 11 (b) shows the scatter plot  
291 between NRMSE-Corrected NeQuick (w.r.t. COSMIC) on x axis and NRMSE-IRI-NeQuick  
292 (w.r.t. COSMIC) on y axis for each individual matched peak profile. It shows that NRMSE-  
293 Corrected NeQuick is lower for nearly half the cases (1803 out of 3433) and NRMSE-IRI-  
294 NeQuick is lower for the rest (1640 out of 3433) but for the majority NRMSE-Corrected  
295 NeQuick is more bounded (from 0 to 0.5) whereas NRMSE-IRI-NeQuick extends from 0 up  
296 to 0.8. Therefore, we can conclude that Corrected-NeQuick is superior to IRI-NeQuick for

297 representing the topside, based on the particular COSMIC dataset under consideration. Klipp  
298 et al., (2020) recently applied the Corrected NeQuick method to study the comparison  
299 between the ionospheric total electron content from ionosondes and the International GNSS  
300 service vertical total electron content and reported that the error was reduced by 27 %.

301 The values of  $r = 100$  and optimised value of  $g = 0.15$  for Corrected NeQuick on DATASET  
302 1 in section (3.1) were also tested for DATASET 2. Figure 12 (a) and (b) show the binned  
303 scatter plot between peak-relative altitude ( $h_{top}$ ) and relative difference ( $RD_{CICN}(h)$ ) between  
304 COSMIC and Corrected NeQuick, for  $h-hmF2 > 100$  and for  $h-hmF2 < 100$ . Figure 12 (a)  
305 clearly shows that the  $RD_{CICN}(h)$  is almost constant with respect to  $h_{top}$  and that it is  
306 confined within a region (-0.2 to 0.2).  $RD_{CICN}(h)$  is also almost 0 for  $h-hmF2 < 100$ , as shown  
307 in Figure 12 (b). By comparing Figure 8, 9, 10 and 12, it is clear that Corrected-NeQuick with  
308 a value of  $g=0.15$  outperforms all other topside formulations for DATASET 2 as well.

### 309 **3.3 Topside scale height linear variation and validation of optimised value of $g = 0.15$** 310 **using DATASET 2.**

311 As discussed in section (3.1) and (3.2), the behaviour of the topside scale height is expected  
312 to be linear. So to verify this for all matched peak COSMIC profiles (3433 profiles in  
313 DATASET 2), the scale height was calculated using equation 24. The scale height of each  
314 profile was fitted under a linear approximation as shown in Figure 13 (a) and subsequently  
315 the corresponding electron density profiles were calculated. Figure 13 (b) shows the relative  
316 difference between measured and modeled electron density (using linearly fitted scale  
317 height). Figure 13 (b) clearly shows that most of the error lies within 5%. This verifies the  
318 linear scale height variation up to 500 km over  $hmF2$  (Pignalberi et al., 2020). The value of  $g$   
319 was also calculated for each of the linear fitted scale height matched peak COSMIC profiles  
320 using equation 7. The results are in line with those obtained by Pignalberi et al., (2020).

321 Figure 14 shows the variation of  $g$  (calculated from equation 7) with respect to RMSE  
322 between COSMIC and linearly fitted scale-height electron density profiles from DATASET  
323 2. It shows that for the majority of the profiles, a value of  $g = 0.15 (\pm 0.015)$  minimises  
324 RMSE. As it was discussed in section (3.1) and (3.2), for an optimum value of  $g = 0.15$ ,  
325 Relative difference between COSMIC and Corrected NeQuick minimises and exhibits the  
326 best performance among all four topside formulations tested on both DATASET 1 and 2.

327

328 **4. Conclusion:**

329 A comparison study between COSMIC topside electron density observations and  $\alpha$ -  
330 Chapman, IRI-NeQuick and Corrected NeQuick estimations has resulted in the following  
331 conclusions:

- 332 1) The overall performance of Corrected NeQuick is superior to IRI-NeQuick, as the  
333 NRMSE introduced by the former is confined (from 0 to 0.5) than the latter (from 0 to  
334 0.8) for the vast majority of cases.
- 335 2) For an optimum value of  $g = 0.15$ ,  $New_g$  Corrected NeQuick performance improves  
336 further. This could be significant, in the context of the single-frequency GNSS  
337 correction algorithm (NeQuick-G) adopted by European Space Agency (ESA) Galileo  
338 GNSS system, as  $r=100$  and  $g=0.125$  are the values embedded in the existing version  
339 of NeQuick-G.
- 340 3) Electron density profiles derived from a linear fitted scale height as extracted from  
341 COSMIC electron density profiles lie within 5% relative difference.
- 342 4) The best linear fit scale height shows that for the optimised value of  $g = 0.15$ , RMSE  
343 is lowest between COSMIC and linearly fitted scale-height electron density profiles

344 **Acknowledgement:**

345 This study was funded by the project “Service for Improving Galileo operation over Cyprus”  
346 (SERVING)-ENTERPRISES/0916/0159 which is co-funded by the Republic of Cyprus and  
347 the European Regional Development Fund (through the 'RESEARCH IN ENTERPRISES'  
348 RESTART 2016-2020 Programme for Research, Technological Development and  
349 Innovation). The authors would like to thank, CDAAC team (COSMIC Data Analysis and  
350 Archive Centre) for the COSMIC/FORMOSAT-3 for making data publicly available via their  
351 website (<https://cdaac-www.cosmic.ucar.edu/cdaac/products.html>). The authors would like to  
352 thank the IRI team for sharing the IRI Model code (<http://irimodel.org/>). The author would  
353 also like to thank Michael Pezzopane and Alessio Pignalberi from the Istituto Nazionale di  
354 Geofisica e Vulcanologia, Italy, for providing access to median values of  $H_{0,AC}$  and  $H_{0,B}$  as a  
355 function of  $foF2$  and  $hmF2$  (Pezzopane & Pignalberi, 2019).

356

357

358

360 **References:**

- 361 1. Anthes, R. A., Bernhardt, P. A., Chen, Y., Cucurull, L., Dymond, K. F., Ector, D.,  
362 Healy, S. B., Ho, S.-P., Hunt, D. C., Kuo, Y.-H., Liu, H., Manning, K., McCormick,  
363 C., Meehan, T. K., Randel, W. J., Rocken, C., Schreiner, W. S., Sokolovskiy, S. V.,  
364 Syndergaard, S., Thompson, D. C., Trenberth, K. E., Wee, T.-K., Yen, N. L., and  
365 Zeng, Z. (2008). "The COSMIC/FORMOSAT-3 Mission: Early Results". *Bull. Amer.*  
366 *Meteor. Soc.*, 89, 313–333. <https://doi.org/10.1175/BAMS-89-3-313>.
- 367 2. Lei, J., Syndergaard, S., Burns, A. G., Solomon, S. C., Wang, W., Zeng, Z., & Zhang,  
368 S. R. (2007). Comparison of COSMIC ionospheric measurements with ground-based  
369 observations and model predictions: Preliminary results. *Journal of Geophysical*  
370 *Research: Space Physics*, 112(A7). <https://doi.org/10.1029/2006JA012240>.
- 371 3. Krankowski, A., Zakharenkova, I., Krypiak-Gregorczyk, A., Shagimuratov, I. I., &  
372 Wielgosz, P. (2011). Ionospheric electron density observed by FORMOSAT-  
373 3/COSMIC over the European region and validated by ionosonde data. *Journal of*  
374 *Geodesy*, 85(12), 949-964. <https://doi.org/10.1007/s00190-011-0481-z>.
- 375 4. Yue, X., Schreiner, W. S., Hunt, D. C., Rocken, C., & Kuo, Y. H. (2011).  
376 Quantitative evaluation of the low Earth orbit satellite based slant total electron  
377 content determination. *Space Weather*, 9(9). <https://doi.org/10.1029/2011SW000687>.
- 378 5. Cherniak, I. V., & Zakharenkova, I. E. (2014). Validation of FORMOSAT-  
379 3/COSMIC radio occultation electron density profiles by incoherent scatter radar  
380 data. *Advances in Space Research*, 53(9), 1304-1312.  
381 <https://doi.org/10.1016/j.asr.2014.02.010>.
- 382 6. Hu, L., Ning, B., Liu, L., Zhao, B., Li, G., Wu, B., & Wu, Z. (2014, October).  
383 Validation of COSMIC ionospheric peak parameters by the measurements of an  
384 ionosonde chain in China. In *Annales Geophysicae* (Vol. 32, No. 10, pp. 1311-1319).  
385 Copernicus GmbH. <https://doi.org/10.5194/angeo-32-1311-2014>.
- 386 7. McNamara, L. F., & Thompson, D. C. (2015). Validation of COSMIC values of foF2  
387 and M(3000)F2 using ground-based ionosondes. *Advances in Space Research*, 55(1),  
388 163-169. <https://doi.org/10.1016/j.asr.2014.07.015>.
- 389 8. Panda, S. K., Haralambous, H., & Kavutarapu, V. (2018). Global Longitudinal  
390 Behavior of IRI Bottomside Profile Parameters From FORMOSAT-3/COSMIC

- 391 Ionospheric Occultations. *Journal of Geophysical Research: Space Physics*, 123(8),  
392 7011-7028. <https://doi.org/10.1029/2018JA025246>.
- 393 9. Shaikh, M. M., Nava, B., & Haralambous, H. (2018). On the Use of Topside RO-  
394 Derived Electron Density for Model Validation. *Journal of Geophysical Research:*  
395 *Space Physics*, 123(5), 3943-3954. <https://doi.org/10.1029/2017JA025132>.
- 396 10. Wang, X., Cheng, W., Zhou, Z., Xu, S., Yang, D., & Cui, J. (2019, November).  
397 Comparison of CSES ionospheric RO data with COSMIC measurements. In *Annales*  
398 *Geophysicae* (Vol. 37, No. 6, pp. 1025-1038). Copernicus GmbH.  
399 <https://doi.org/10.5194/angeo-37-1025-2019>.
- 400 11. Bai, W., Tan, G., Sun, Y., Xia, J., Cheng, C., Du, Q., ...& Meng, X. (2019).  
401 Comparison and validation of the ionospheric climatological morphology of  
402 FY3C/GNOS with COSMIC during the recent low solar activity period. *Remote*  
403 *Sensing*, 11(22), 2686. <https://doi.org/10.3390/rs11222686>.
- 404 12. Rishbeth, H., & Garriott, O. K. (1969). *Introduction to ionospheric physics* (Vol. 14).  
405 New York: Academic Press.
- 406 13. Hargreaves, J. K. (1992). *The solar-terrestrial environment: an introduction to*  
407 *geospace-the science of the terrestrial upper atmosphere, ionosphere, and*  
408 *magnetosphere*. Cambridge university press.
- 409 14. Liu, L., Le, H., Wan, W., Sulzer, M. P., Lei, J., & Zhang, M. L. (2007a). An analysis  
410 of the scale heights in the lower topside ionosphere based on the Arecibo incoherent  
411 scatter radar measurements. *Journal of Geophysical Research: Space*  
412 *Physics*, 112(A6). <https://doi.org/10.1029/2007JA012250>.
- 413 15. Liu, L., Wan, W., Zhang, M. L., Ning, B., Zhang, S. R., & Holt, J. M. (2007b).  
414 Variations of topside ionospheric scale heights over Millstone Hill during the 30-day  
415 incoherent scatter radar experiment. <https://hal.archives-ouvertes.fr/hal-00318384>.
- 416 16. Bilitza, D., Altadill, D., Truhlik, V., Shubin, V., Galkin, I., Reinisch, B., & Huang, X.  
417 (2017). International Reference Ionosphere 2016: From ionospheric climate to real-  
418 time weather predictions. *Space Weather*, 15(2), 418-429.  
419 <https://doi.org/10.1002/2016SW001593>.
- 420 17. Bilitza, D. (1990). *International Reference Ionosphere 1990*, National Space Science  
421 Data Center. NSSDC/WDC-AR &S 90-22.
- 422 18. Bilitza, D. (2004). A correction for the IRI topside electron density model based on  
423 Alouette/ISIS topside sounder data. *Advances in Space Research*, 33(6), 838-843.  
424 <https://doi.org/10.1016/j.asr.2003.07.009>.

- 425 19. Radicella, S. M., & Leitinger, R. (2001). The evolution of the DGR approach to  
426 model electron density profiles. *Advances in Space Research*, 27(1), 35-40.  
427 [https://doi.org/10.1016/S0273-1177\(00\)00138-1](https://doi.org/10.1016/S0273-1177(00)00138-1).
- 428 20. Coisson, P., Radicella, S. M., Leitinger, R., & Nava, B. (2006). Topside electron  
429 density in IRI and NeQuick: Features and limitations. *Advances in Space  
430 Research*, 37(5), 937-942. <https://doi.org/10.1016/j.asr.2005.09.015>.
- 431 21. Nava, B., Coisson, P., & Radicella, S. M. (2008). A new version of the NeQuick  
432 ionosphere electron density model. *Journal of Atmospheric and Solar-Terrestrial  
433 Physics*, 70(15), 1856-1862. <https://doi.org/10.1016/j.jastp.2008.01.015>.
- 434 22. Bilitza, D. (2009). Evaluation of the IRI-2007 model options for the topside electron  
435 density. *Advances in space research*, 44(6), 701-706.  
436 <https://doi.org/10.1016/j.asr.2009.04.036>.
- 437 23. Bilitza, D., Reinisch, B. W., Radicella, S. M., Pulnits, S., Gulyaeva, T., & Triskova,  
438 L. (2006). Improvements of the International Reference Ionosphere model for the  
439 topside electron density profile. *Radio science*, 41(05), 1-8.  
440 <https://doi.org/10.1029/2005RS003370>.
- 441 24. Pignalberi, A., Pezzopane, M., Tozzi, R., De Michelis, P., & Coco, I. (2016).  
442 Comparison between IRI and preliminary Swarm Langmuir probe measurements  
443 during the St. Patrick storm period. *Earth, Planets and Space*, 68(1), 93.  
444 <https://doi.org/10.1186/s40623-016-0466-5>.
- 445 25. Pezzopane, M., & Pignalberi, A. (2019). The ESA Swarm mission to help ionospheric  
446 modeling: a new NeQuick topside formulation for mid-latitude regions. *Scientific  
447 reports*, 9(1), 1-12. <https://doi.org/10.1038/s41598-019-48440-6>.
- 448 26. Pignalberi, A., Pietrella, M., Pezzopane, M., & Rizzi, R. (2018). Improvements and  
449 validation of the IRI UP method under moderate, strong, and severe geomagnetic  
450 storms. *Earth, Planets and Space*, 70(1), 180. [https://doi.org/10.1186/s40623-018-  
451 0952-z](https://doi.org/10.1186/s40623-018-0952-z).
- 452 27. Schreiner, W.S., Sokolovskiy, S.V., Rocken, C. and Hunt, D.C. (1999). Analysis and  
453 validation of GPS/MET radio occultation data in the ionosphere. *Radio  
454 Science*, 34(4), pp.949-966. <https://doi.org/10.1029/1999RS900034>.
- 455 28. Stankov, S. M., & Jakowski, N. (2006). Topside ionospheric scale height analysis and  
456 modelling based on radio occultation measurements. *Journal of atmospheric and  
457 solar-terrestrial physics*, 68(2), 134-162. <https://doi.org/10.1016/j.jastp.2005.10.003>.

- 458 29. Themens, D. R., Jayachandran, P. T., Bilitza, D., Erickson, P. J., Häggström, I.,  
459 Lyashenko, M. V., & Pustovalova, L. (2018). Topside electron density representations  
460 for middle and high latitudes: A topside parameterization for E-CHAIM based on the  
461 NeQuick. *Journal of Geophysical Research: Space Physics*, 123(2), 1603-1617.  
462 <https://doi.org/10.1002/2017JA024817>.
- 463 30. Themens, D. R., Jayachandran, P. T., Nicolls, M. J., & MacDougall, J. W. (2014). A  
464 top to bottom evaluation of IRI 2007 within the polar cap. *Journal of Geophysical*  
465 *Research: Space Physics*, 119(8), 6689-6703. <https://doi.org/10.1002/2014JA020052>.
- 466 31. Pignalberi, A., Pezzopane, M., Themens, D. R., Haralambous, H., Nava, B., &  
467 Coisson, P. (2020). On the Analytical Description of the Topside Ionosphere by  
468 NeQuick: Modeling the Scale Height Through COSMIC/FORMOSAT-3 Selected  
469 Data. *IEEE Journal of Selected Topics in Applied Earth Observations and Remote*  
470 *Sensing*, 13, 1867-1878. [10.1109/JSTARS.2020.2986683](https://doi.org/10.1109/JSTARS.2020.2986683).
- 471 32. Olivares-Pulido, G., Hernández-Pajares, M., Aragón-Ángel, A., & Garcia-Rigo, A.  
472 (2016). A linear scale height Chapman model supported by GNSS occultation  
473 measurements. *Journal of Geophysical Research: Space Physics*, 121(8), 7932-7940.  
474 <https://doi.org/10.1002/2016JA022337>.
- 475 33. Klipp, T. D. S., Petry, A., Souza, J. R. D., Paula, E. R. D., Falcão, G. S., & Campos  
476 Velho, H. F. D. (2020, March). Ionosonde total electron content evaluation using  
477 International Global Navigation Satellite System Service data. In *Annales*  
478 *Geophysicae* (Vol. 38, No. 2, pp. 347-357). Copernicus GmbH.  
479 <https://doi.org/10.5194/angeo-38-347-2020>.

480

481

482

483

484

485

486

487

488 **Table captions:**

489 **Table 1:** The Ionosonde stations name (Country) collocated with the COSMIC RO profiles  
490 with their location (geographic latitude, longitude), geomagnetic latitude, Number of  
491 coincident observations and Number of Matched Peak Profiles.

492 **Figure Caption:**

493 **Figure 1:** The graph shows the COSMIC RO profile variation with respect to Latitude (on y  
494 axis) and Longitude (on x-axis) and Nearest Digisonde station which meets the topside  
495 coincident criteria.

496 **Figure 2:** The graph shows the binscatter plot of (a) Relative difference ( $RD_{CD}$ ) between  
497 COSMIC observations and  $\alpha$ -Chapman estimations (b) Scale height of  $\alpha$ -Chapman  
498 estimations as a function of peak-relative altitude ( $h-hmF2$ ).

499 **Figure 3:** The graph shows the binscatter plot of (a) Relative difference ( $RD_{CIRI}$ ) between  
500 COSMIC observations and IRI-NeQuick estimations (b) Scale height of IRI-NeQuick  
501 estimations as a function of peak-relative altitude ( $h-hmF2$ ).

502 **Figure 4:** The graph shows the binscatter plot of (a) Relative difference ( $RD_{CCN}$ ) between  
503 COSMIC observations and Corrected NeQuick estimations (b) Scale height of Corrected  
504 NeQuick estimations as a function of peak-relative altitude ( $h-hmF2$ ).

505 **Figure 5:** The graph shows the binscatter plot of Scale height of COSMIC observations as a  
506 function of peak-Relative altitude ( $h-hmF2$ ).

507 **Figure 6:** The graph shows the contour plot of RMSE between COSMIC observations and  
508 Corrected NeQuick estimations for varying value of r and g.

509 **Figure 7:** The graph shows the binscatter plot of (a) Relative difference ( $RD_{CICN}$ ) between  
510 COSMIC observations and  $New_g$  Corrected estimations (b) Scale height of  $New_g$  Corrected  
511 estimations as a function of peak-relative altitude ( $h-hmF2$ ).

512 **Figure 8:** The graph shows the binscatter plot of relative difference ( $RD_{CD}$  (h)) between  
513 COSMIC observed and  $\alpha$ -Chapman estimated matched peak electron density profiles for (a)  
514  $h-hmF2 > 100$  (b)  $h-hmF2 < 100$  as a function of peak-relative altitude ( $h-hmF2$ ).

515 **Figure 9:** The graph shows the binscatter plot of relative difference ( $RD_{CIRI}$  (h)) between  
516 COSMIC observed and IRI-NeQuick estimated matched peak electron density profiles for (a)  
517  $h-hmF2 > 100$  (b)  $h-hmF2 < 100$  as a function of peak-relative altitude ( $h-hmF2$ ).

518 **Figure 10:** The graph shows the binscatter plot of relative difference ( $RD_{CCN}(h)$ ) between  
519 COSMIC observed and Corrected NeQuick estimated matched peak electron density profiles  
520 for (a)  $h-hmF2 > 100$  (b)  $h-hmF2 < 100$  as a function of peak-relative altitude ( $h-hmF2$ ).

521 **Figure 11:** The graph shows the scatter plot between the NRMSE\_Corrected NeQuick (a)  
522 NRMSE\_  $\alpha$ -Chapman (b) NRMSE\_IRI-NeQuick for matched peak profiles. The Red line  
523 shows the  $y=x$  line on the graph.

524 **Figure 12:** The graph shows the binscatter plot of relative difference ( $RD_{CICN}(h)$ ) between  
525 COSMIC observed and New<sub>g</sub> Corrected NeQuick estimated matched peak electron density  
526 profiles for (a)  $h-hmF2 > 100$  (b)  $h-hmF2 < 100$  as a function of peak-relative altitude ( $h-hmF2$ ).

527 **Figure 13:** The graph shows the (a) variation of Scale height inverted from COSMIC profile  
528 (blue dots) and red line shows the best linear fit line (b) Relative difference between the  
529 COSMIC matched peak profiles and corresponding linear fitted profiles as a function of  
530 peak-relative altitude ( $h-hmF2$ ).

531 **Figure 14:** The graph shows the RMSE between the COSMIC matched peak profiles and  
532 corresponding linear fitted profiles with respect to the slope of best linear fit line (g).

Figure 1.

# COSMIC RO profile projection coincident with nearest digisonde station at topside

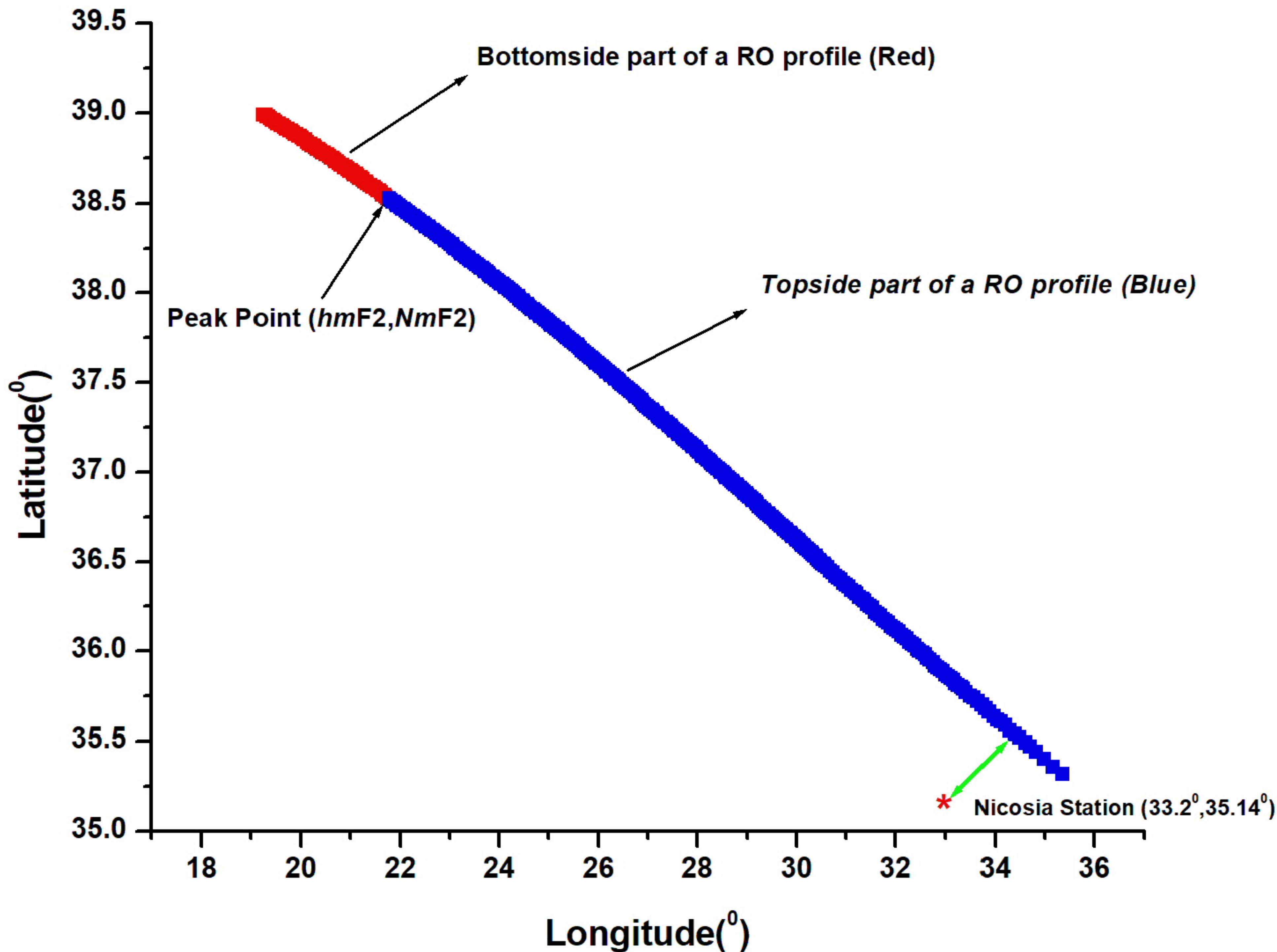
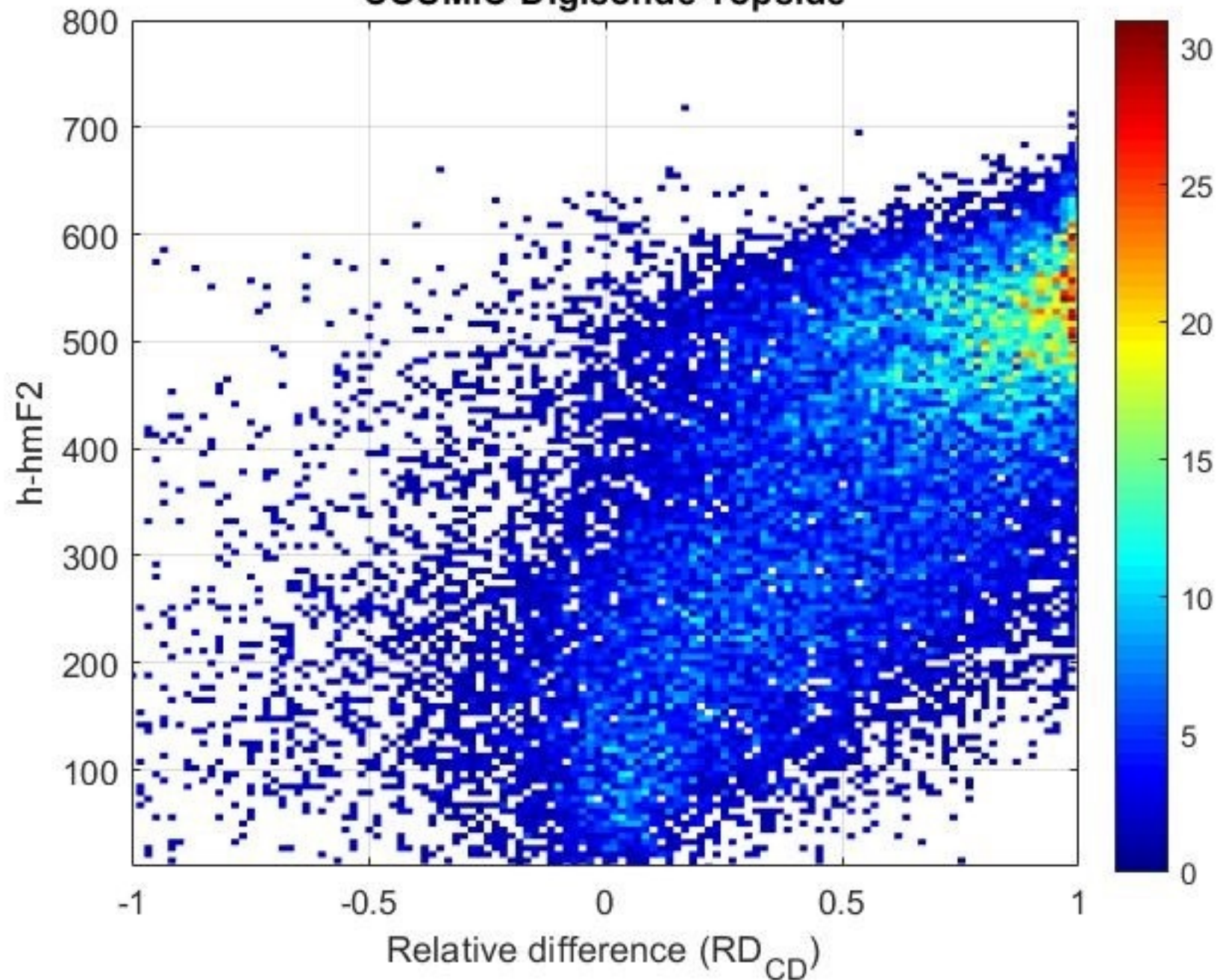


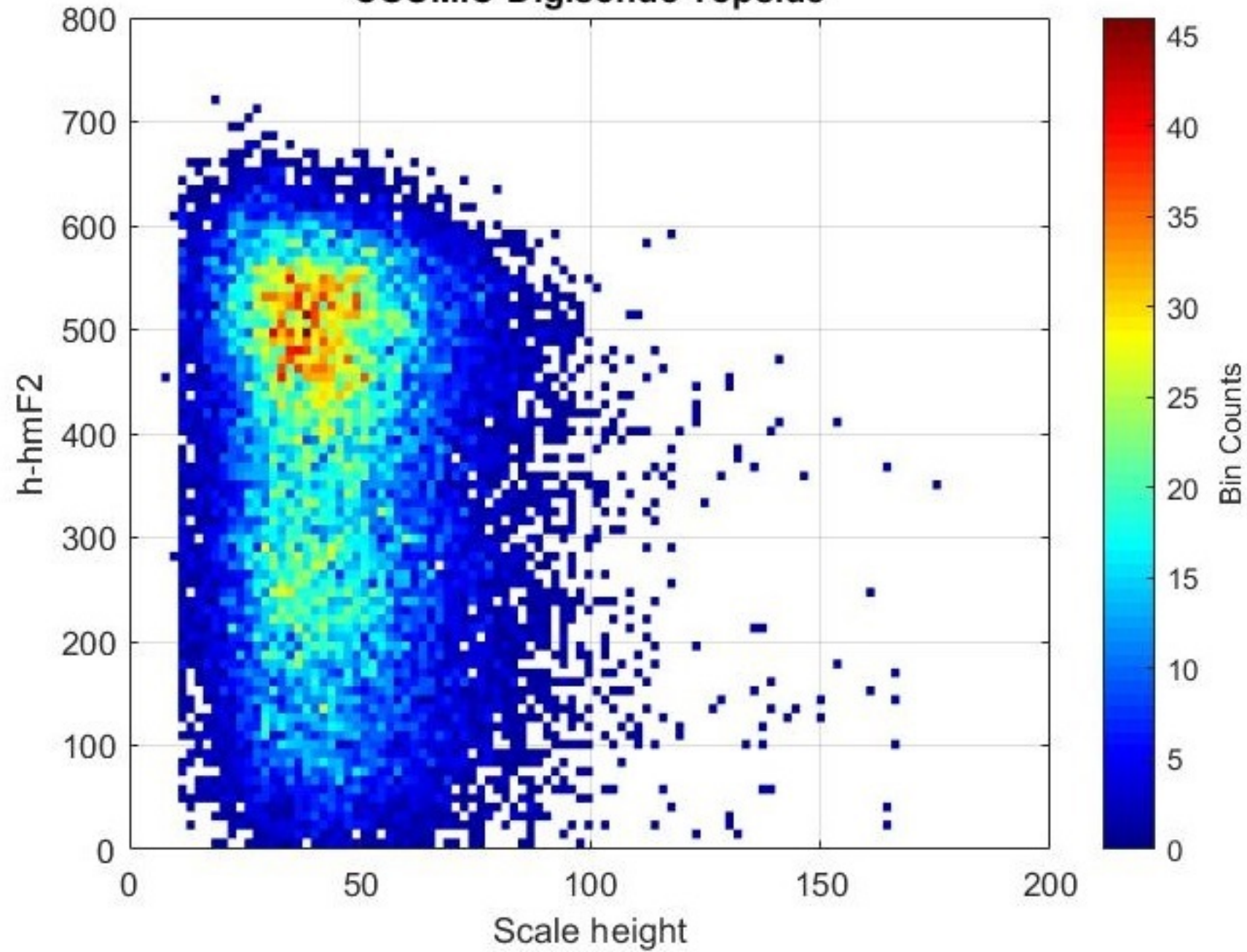
Figure 2.

COSMIC-Digisonde Topside



(a)

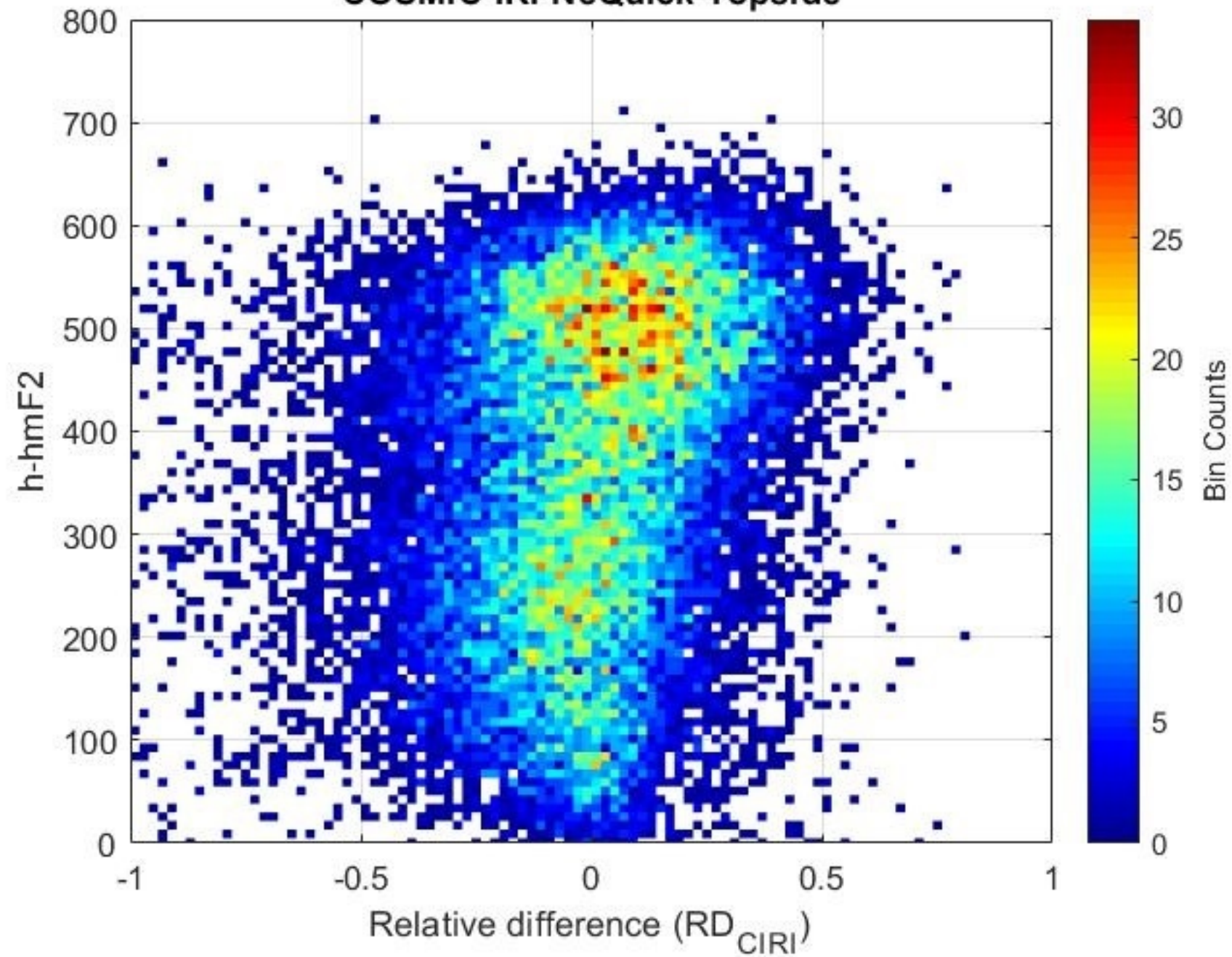
COSMIC-Digisonde Topside



(b)

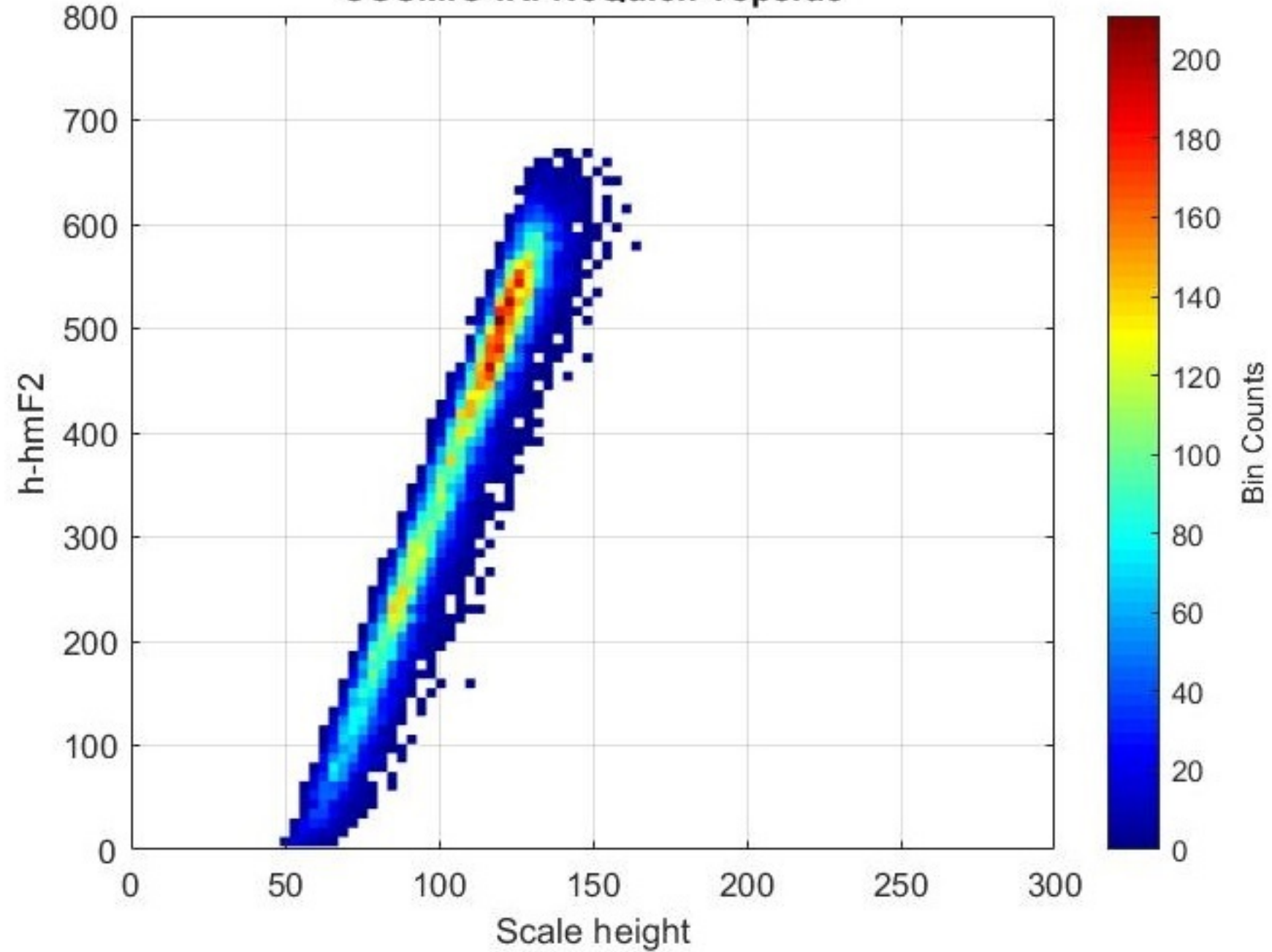
Figure 3.

COSMIC-IRI-NeQuick Topside



(a)

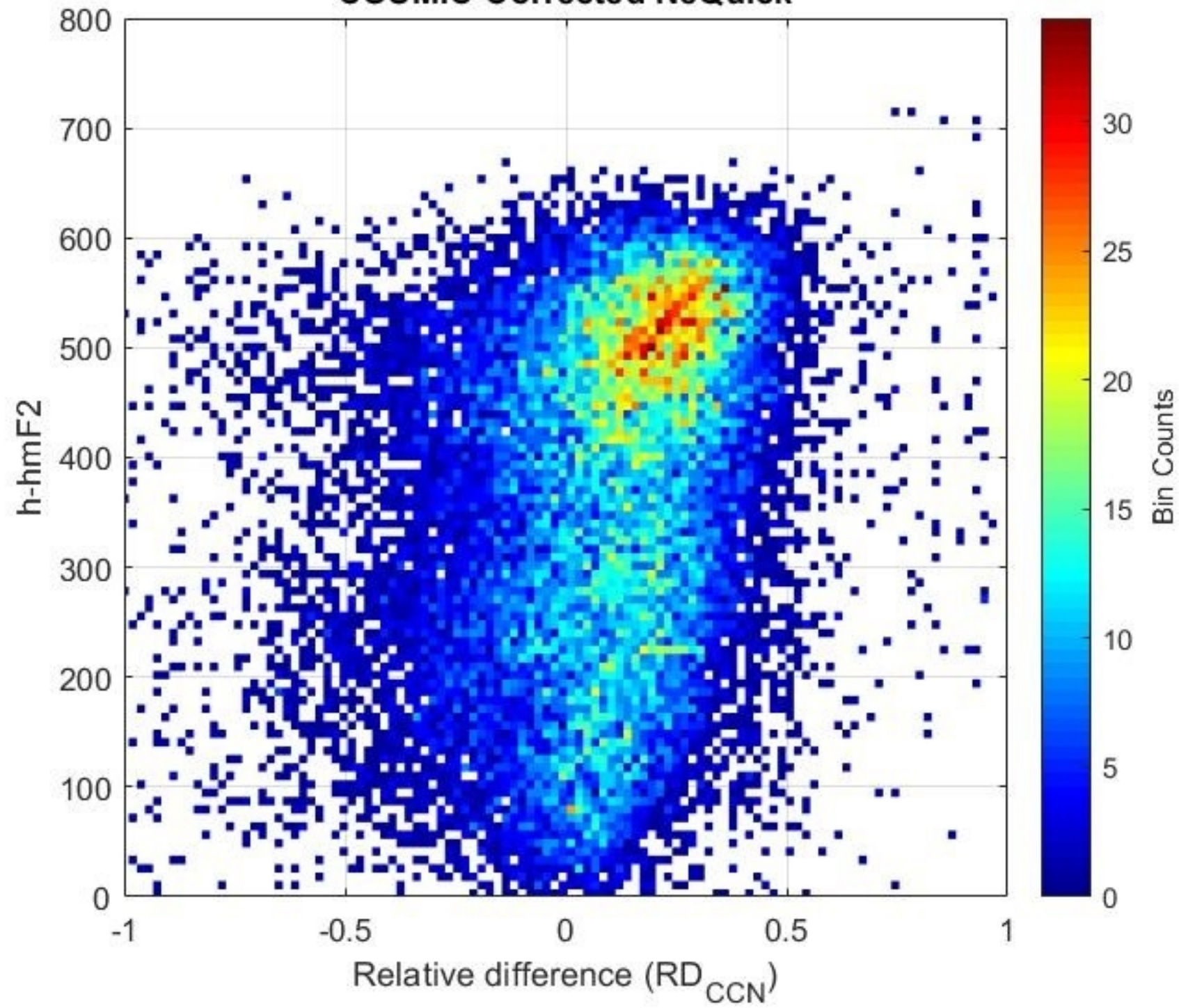
COSMIC-IRI-NeQuick Topside



(b)

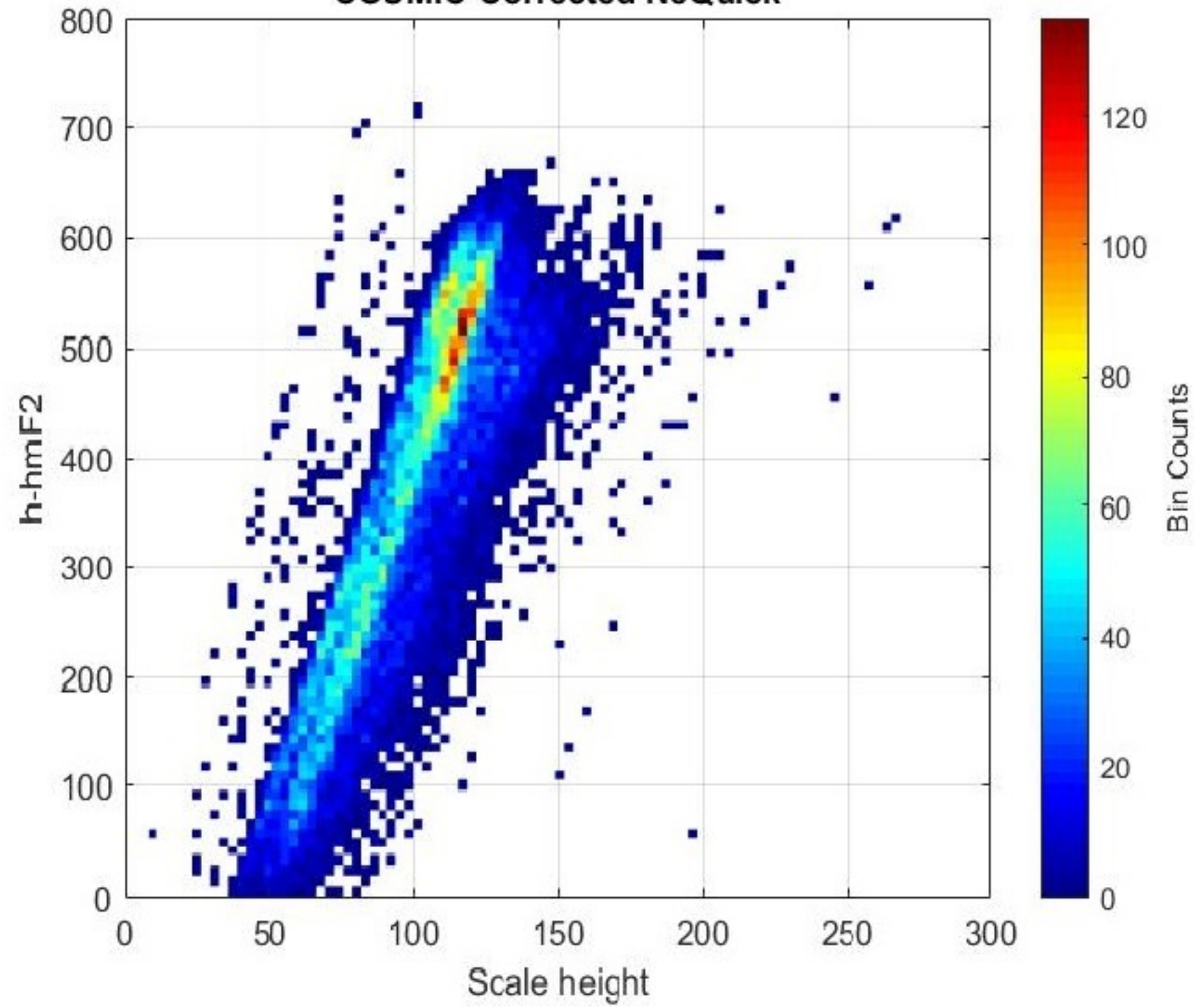
**Figure 4.**

COSMIC-Corrected NeQuick



(a)

COSMIC-Corrected NeQuick



(b)

Figure 5.

# COSMIC

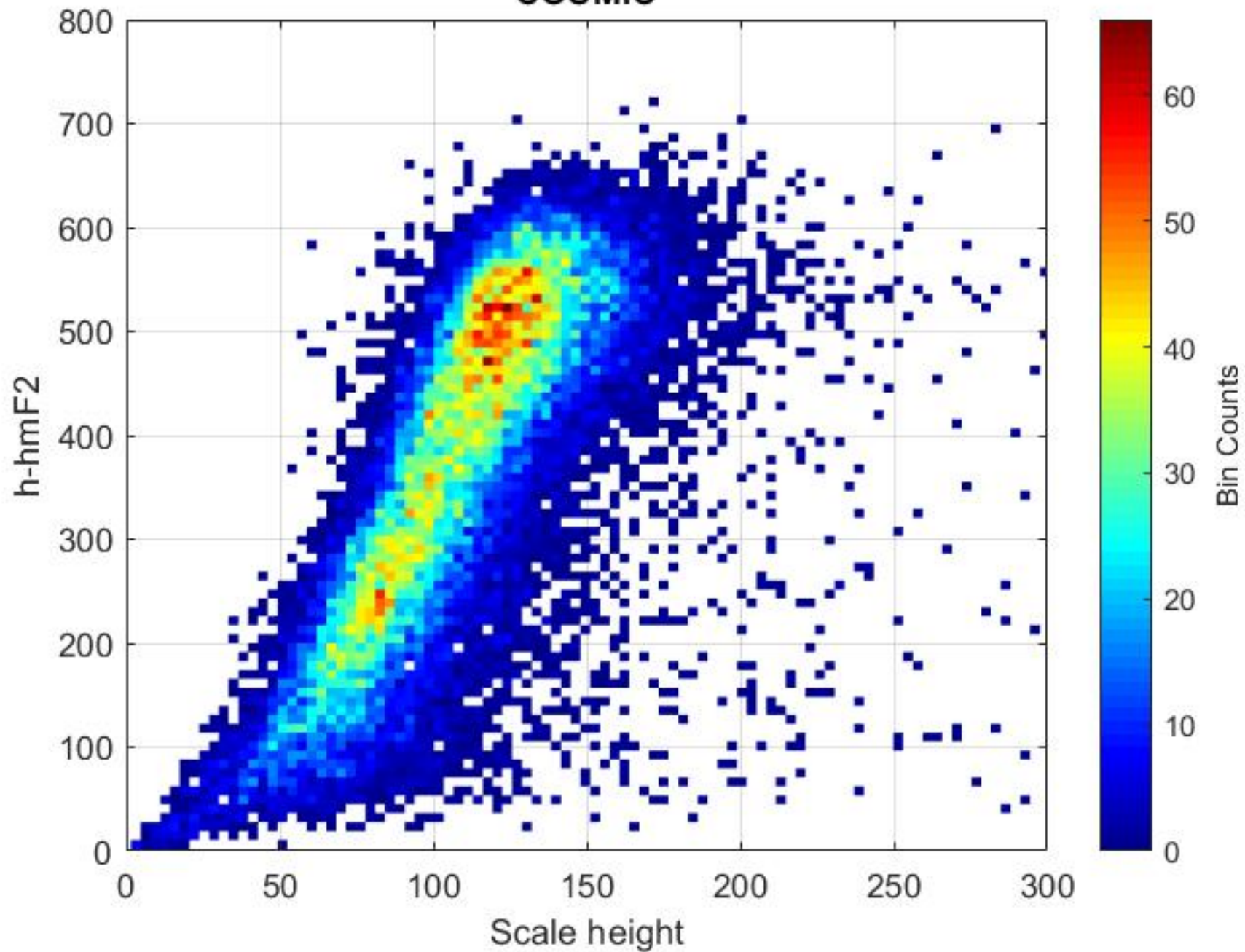
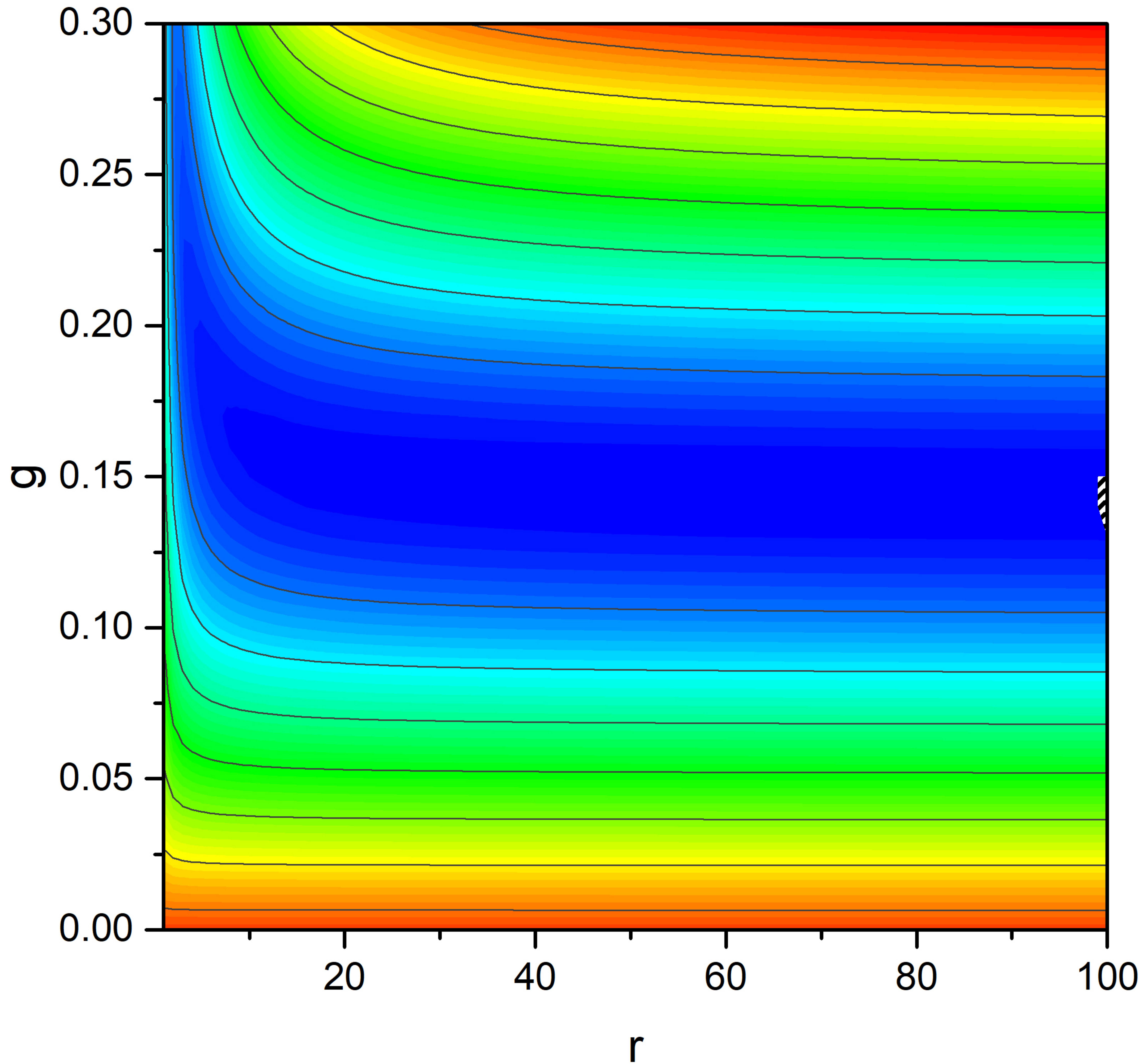


Figure 6.

# COSMIC-Corrected NeQuick



RMSE

62.60

57.03

51.45

45.88

40.30

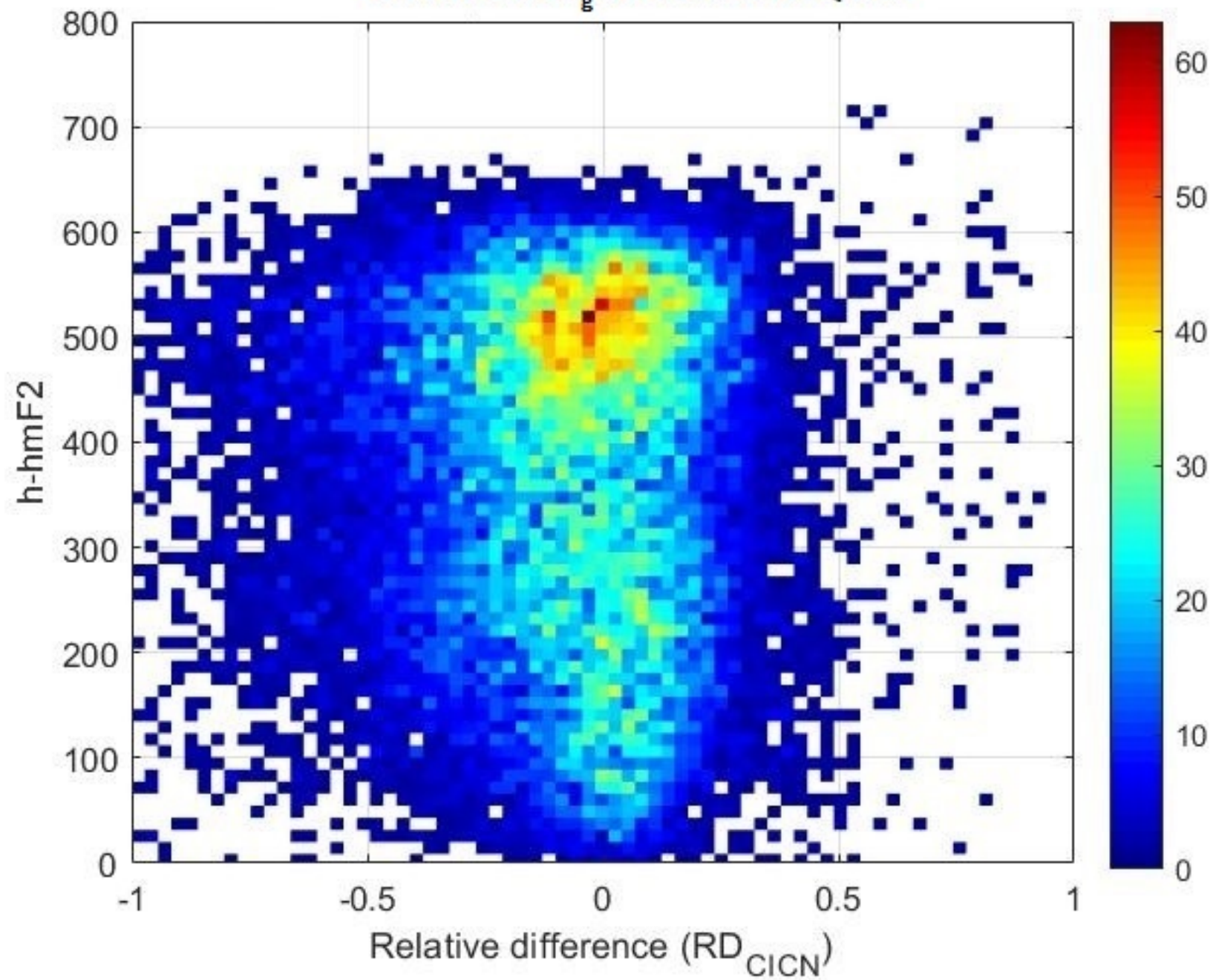
34.73

29.15

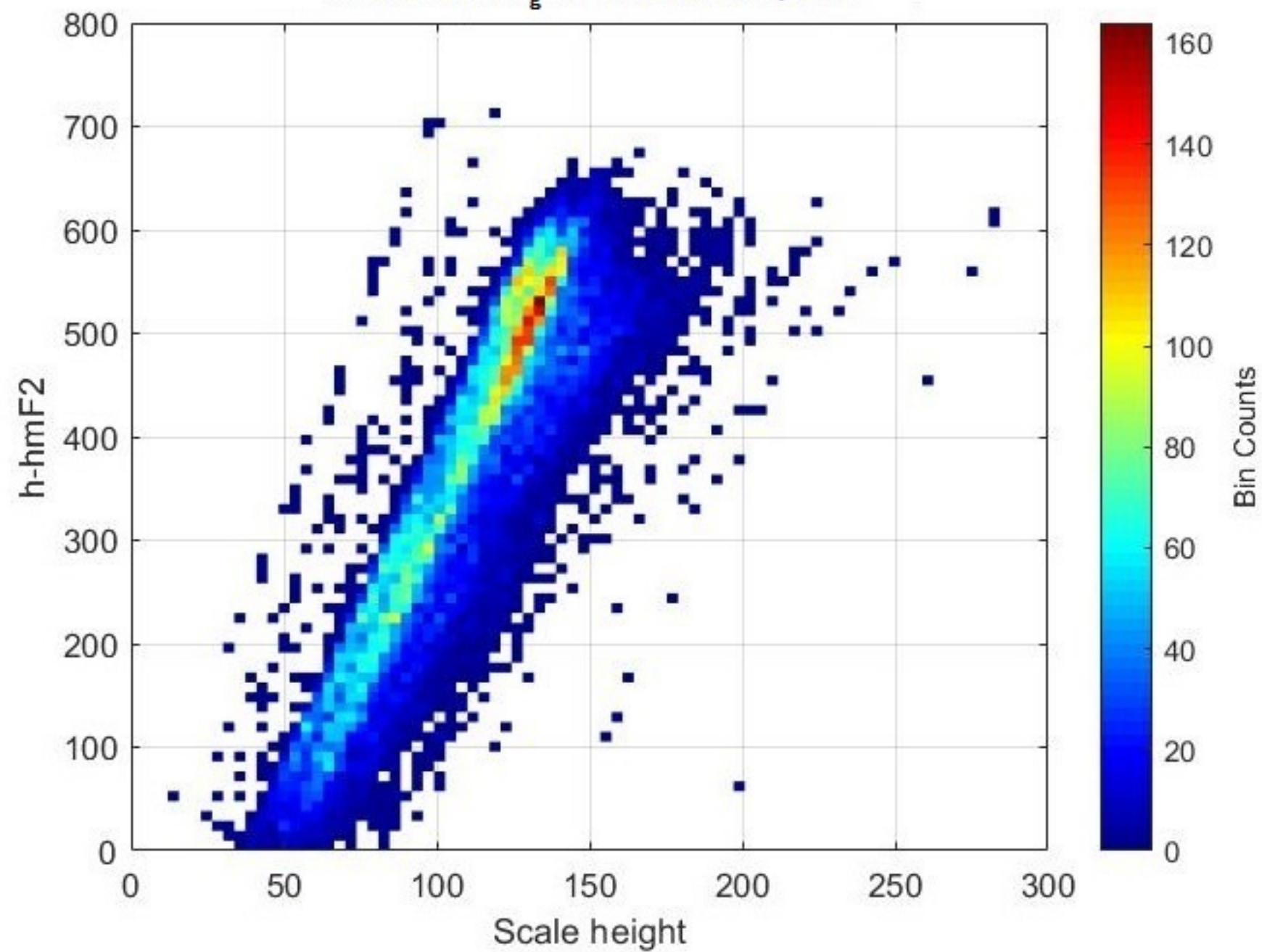
23.58

18.00

Figure 7.

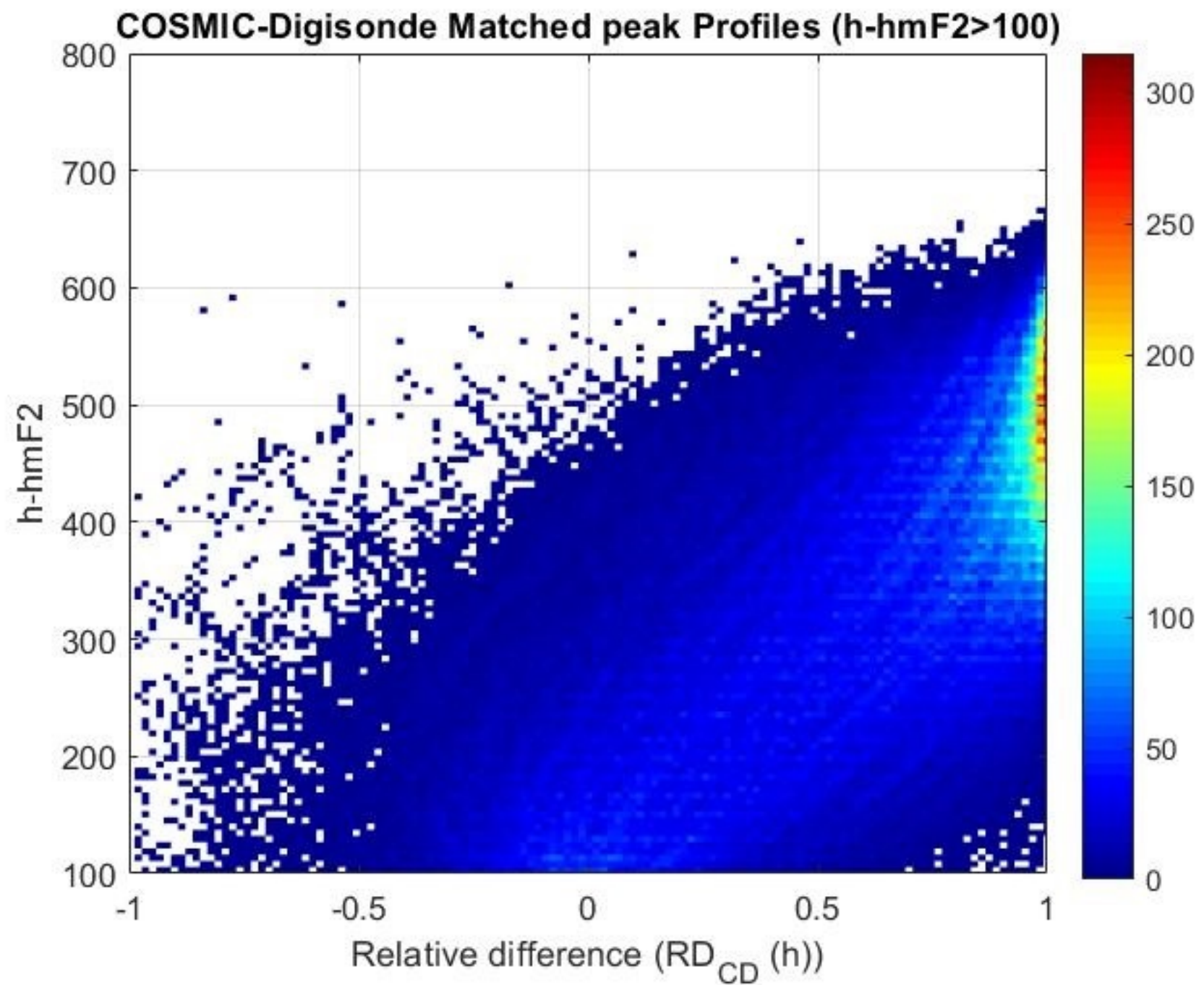
COSMIC New<sub>g</sub> Corrected NeQuick

(a)

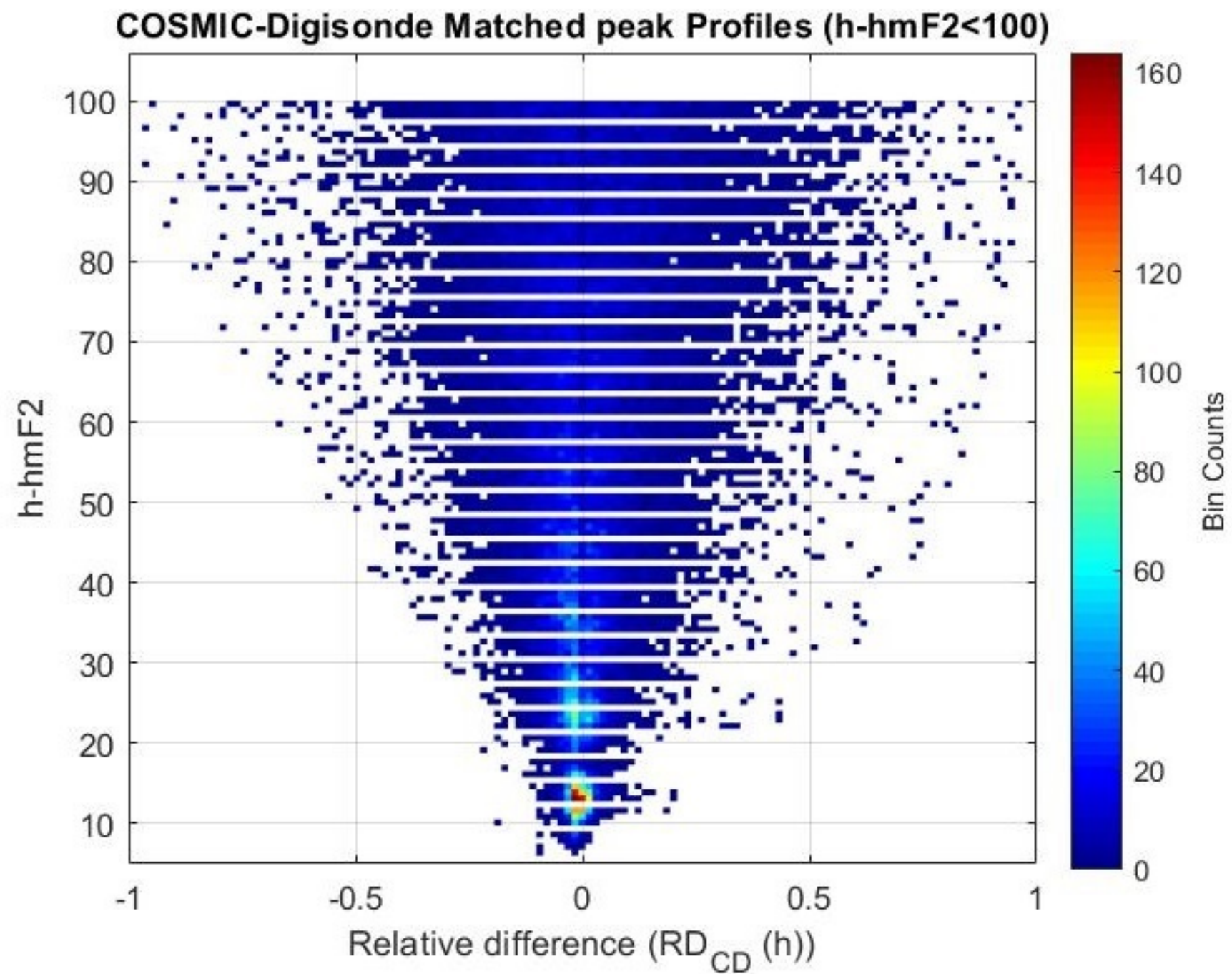
COSMIC New<sub>g</sub> Corrected NeQuick

(b)

Figure 8.



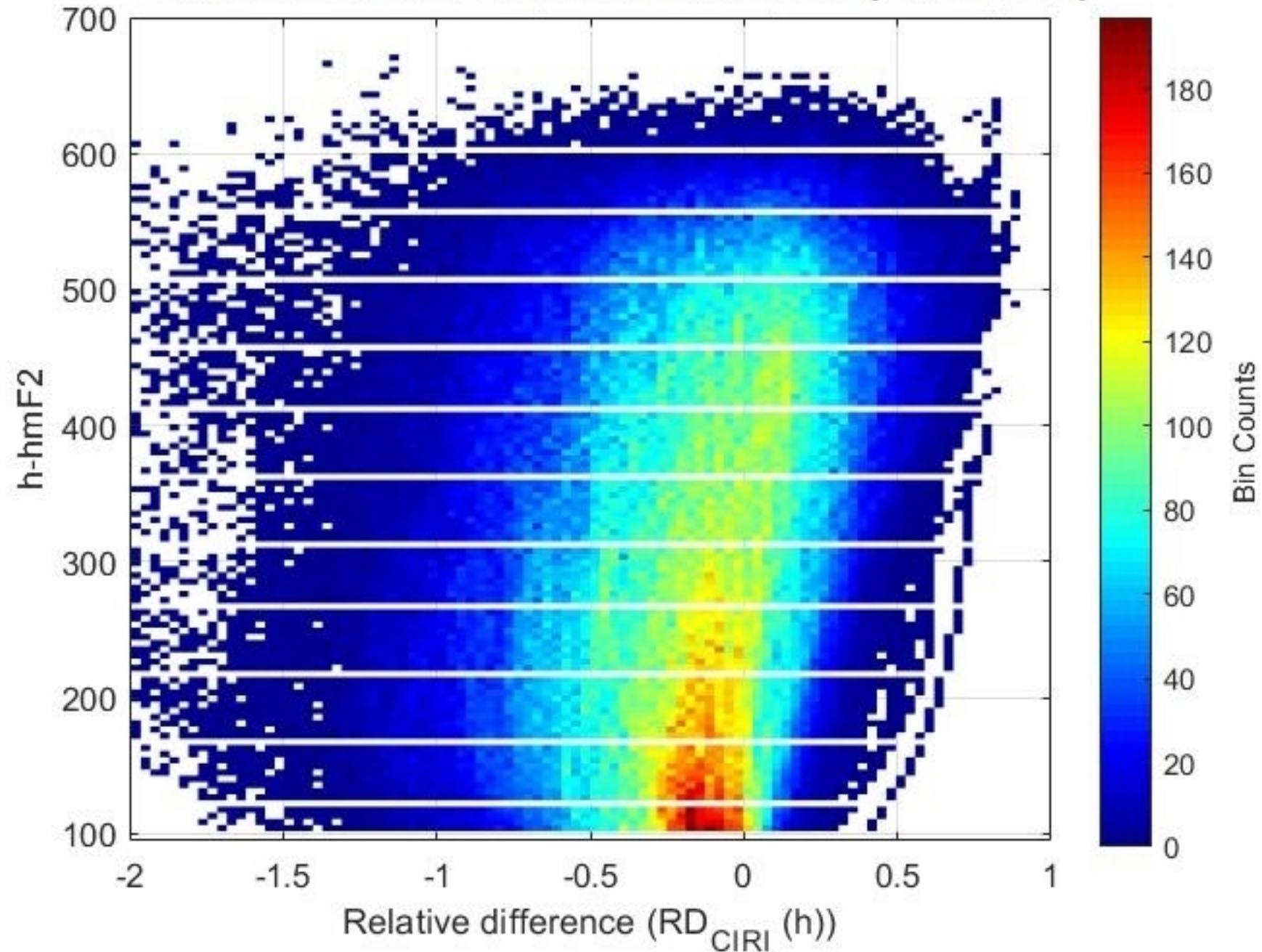
**(a)**



**(b)**

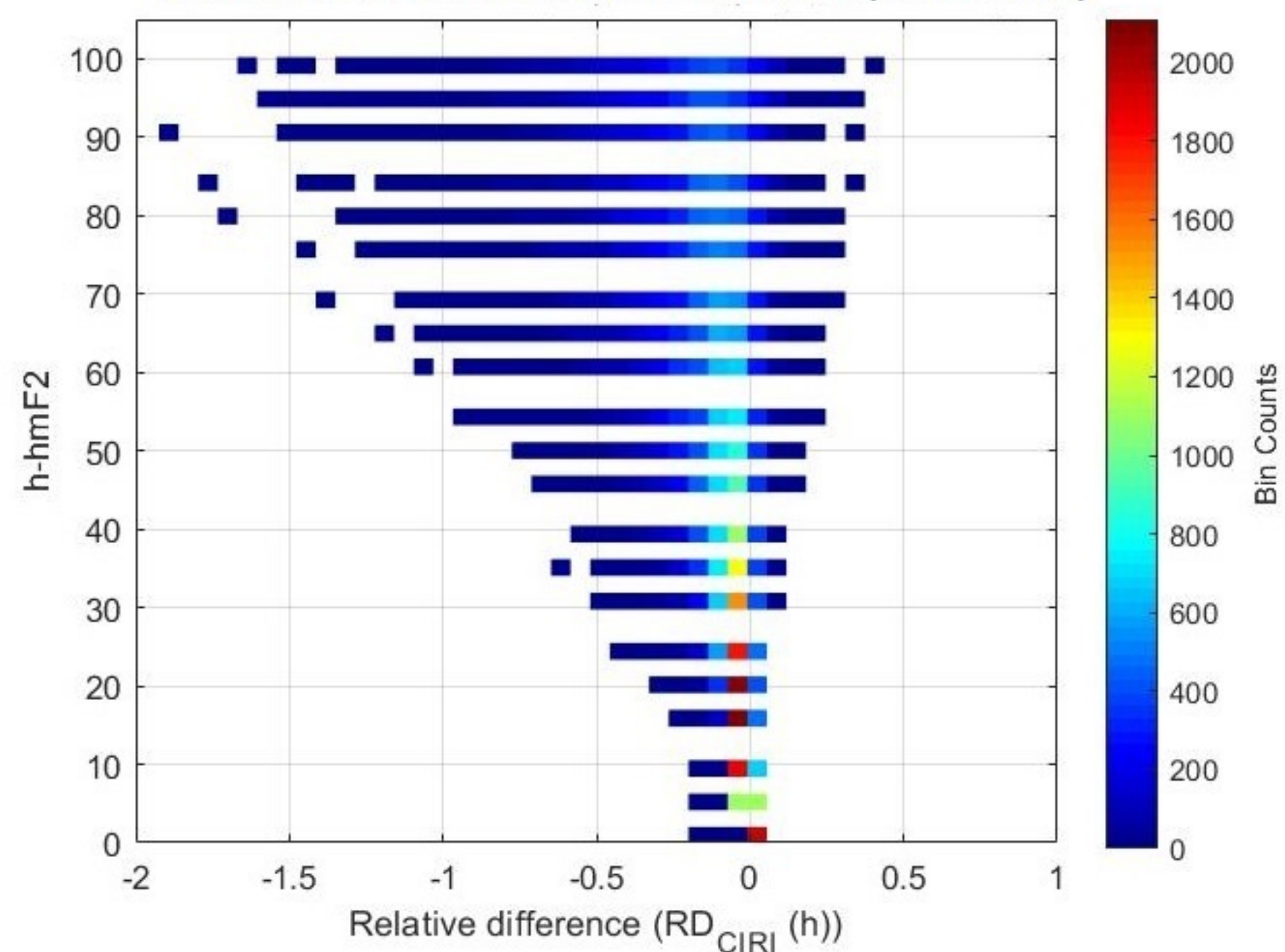
Figure 9.

COSMIC-IRI-NeQuick Matched Peak Profiles ( $h\text{-hmF2} > 100$ )



(a)

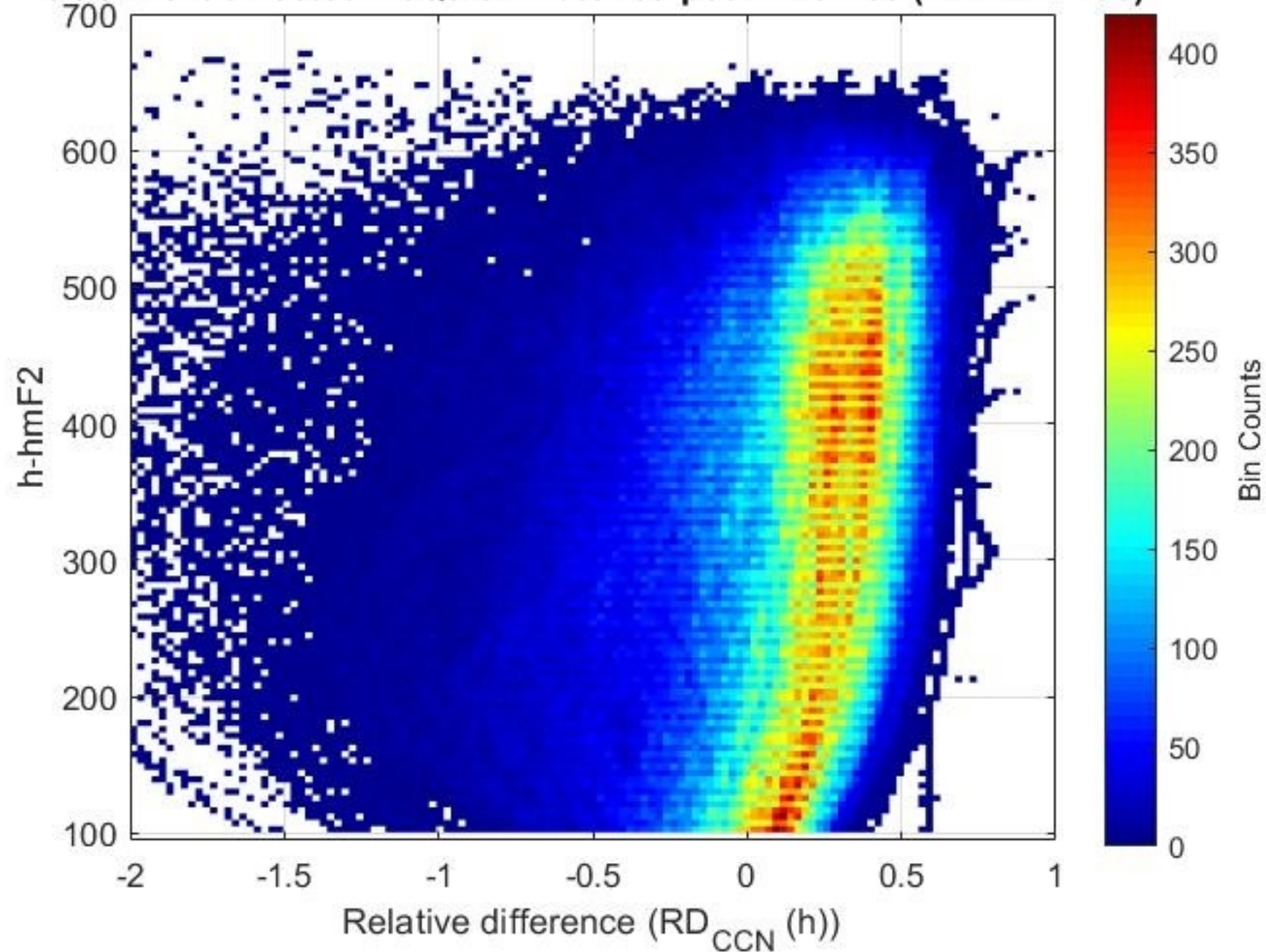
COSMIC-IRI-NeQuick Matched Peak Profiles ( $h\text{-hmF2} < 100$ )



(b)

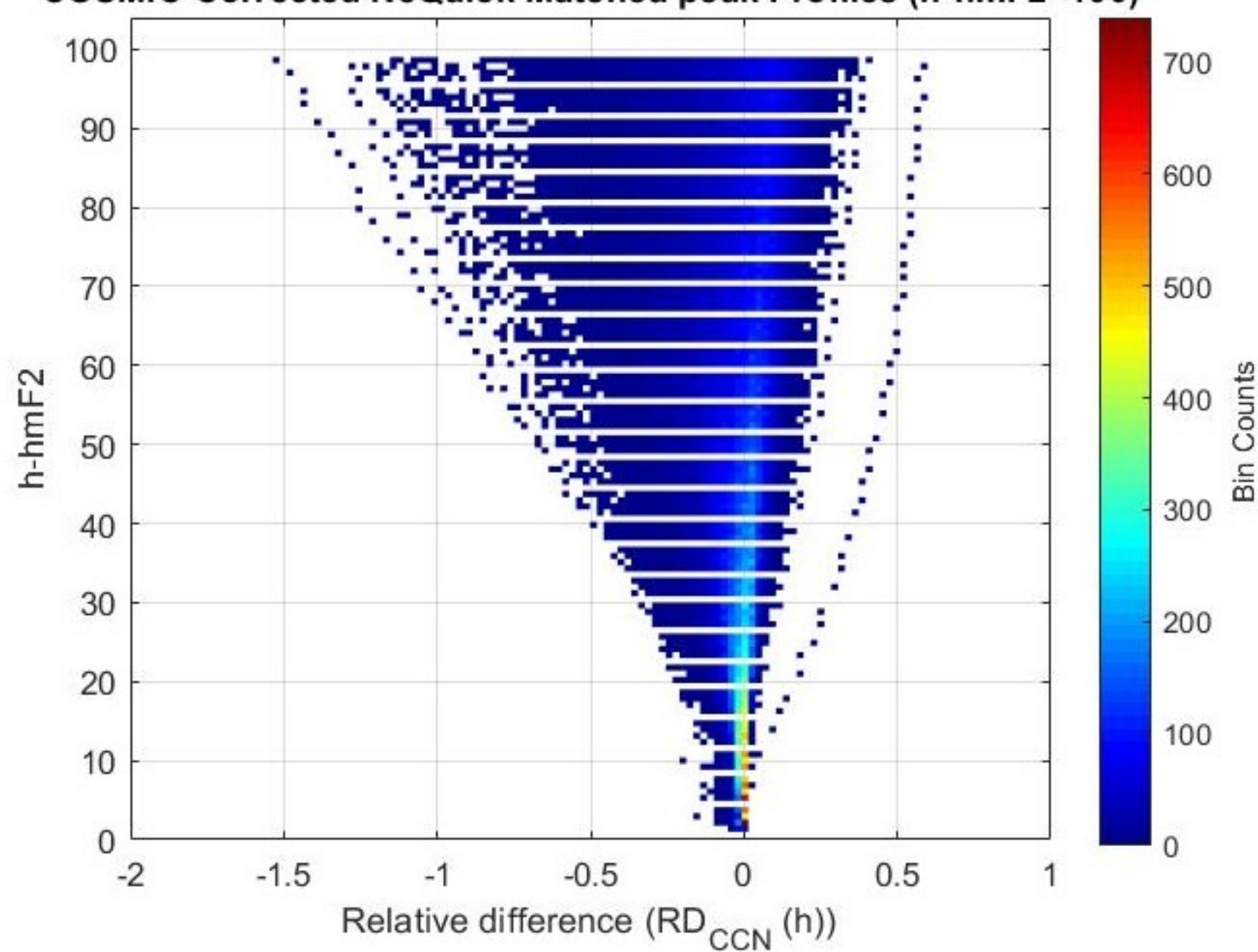
Figure 10.

COSMIC-Corrected NeQuick Matched peak Profiles ( $h\text{-hmF2} > 100$ )



(a)

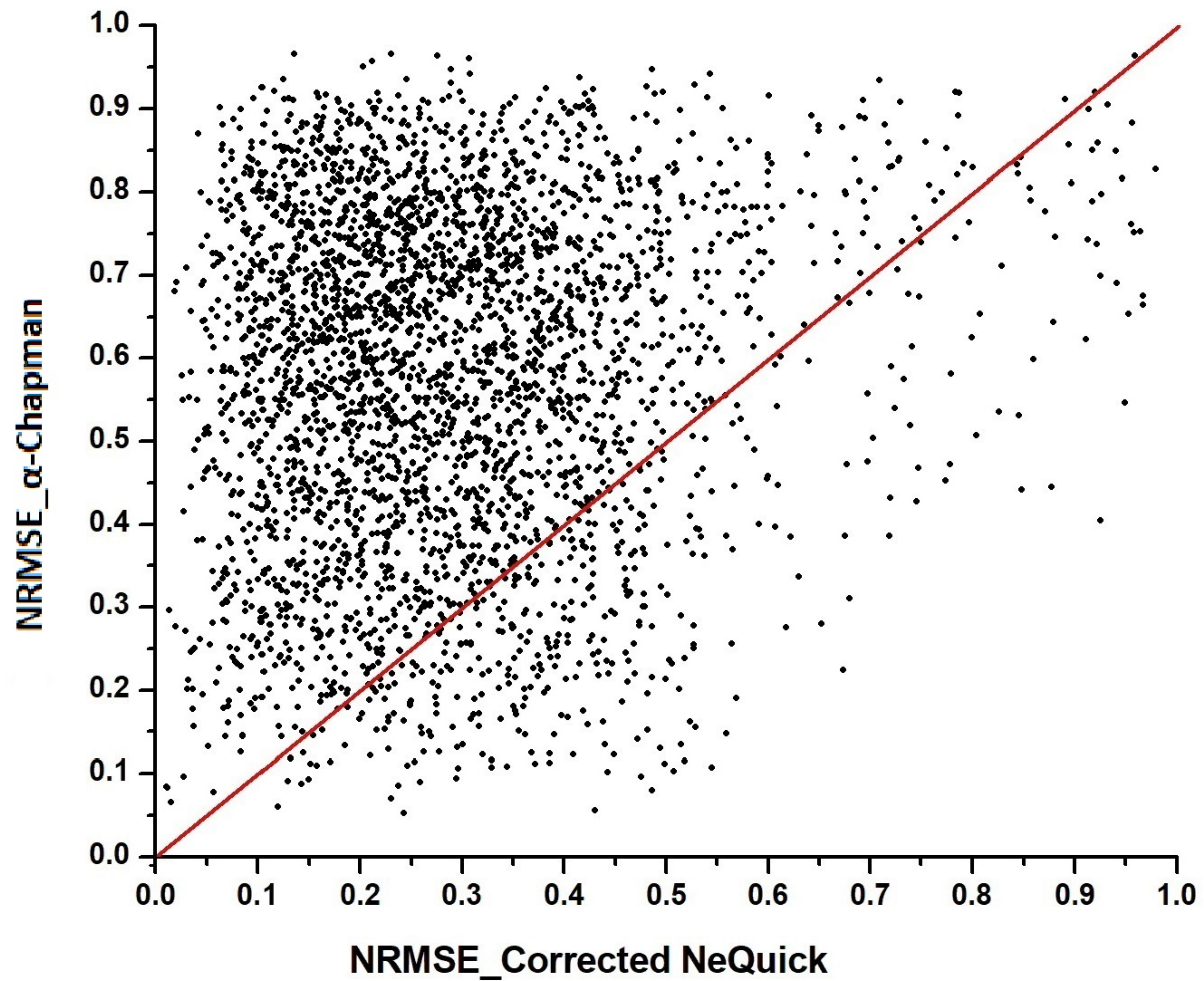
COSMIC-Corrected NeQuick Matched peak Profiles ( $h\text{-hmF2} < 100$ )



(b)

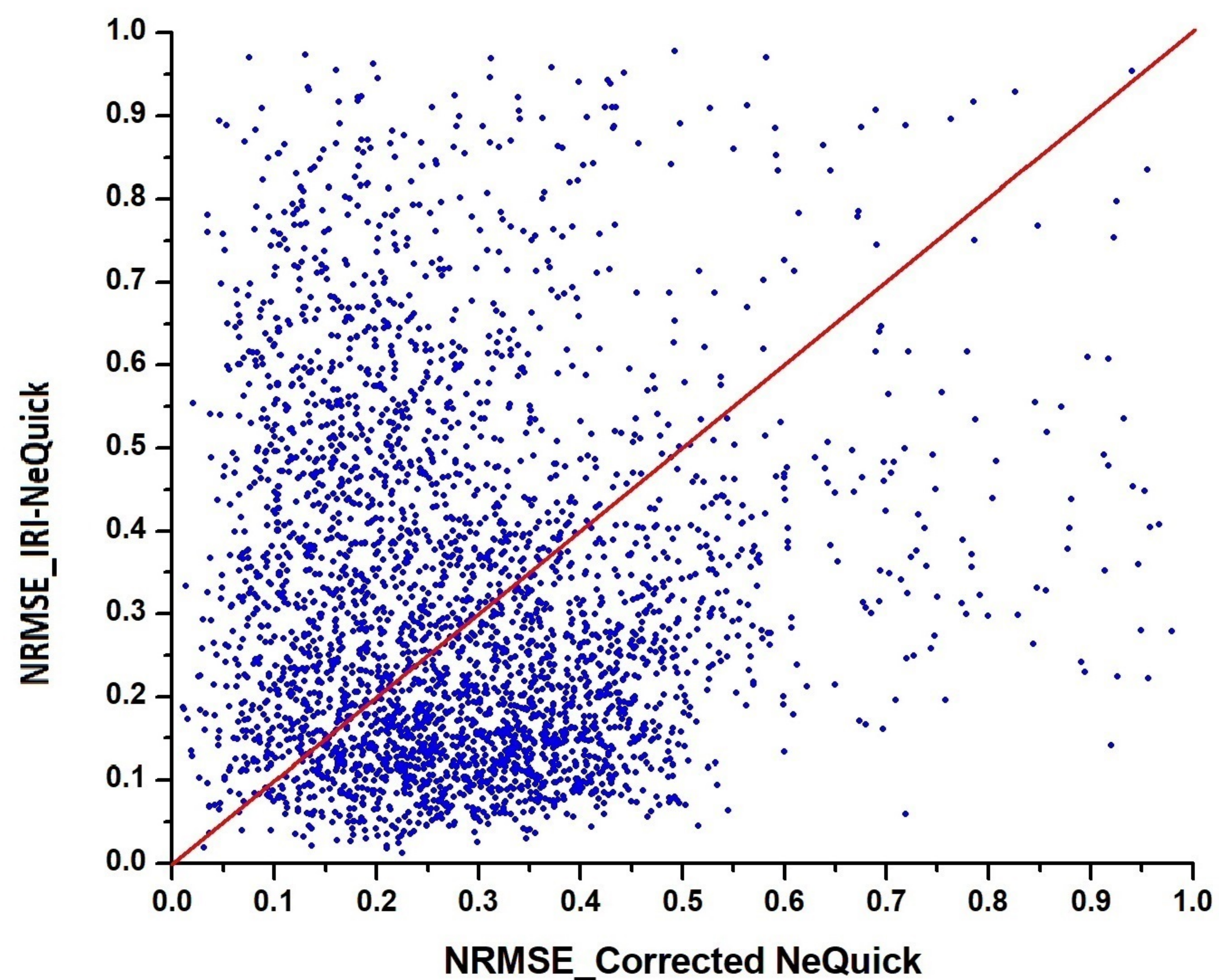
Figure 11.

NRMSE for Matched Peak Profile



(a)

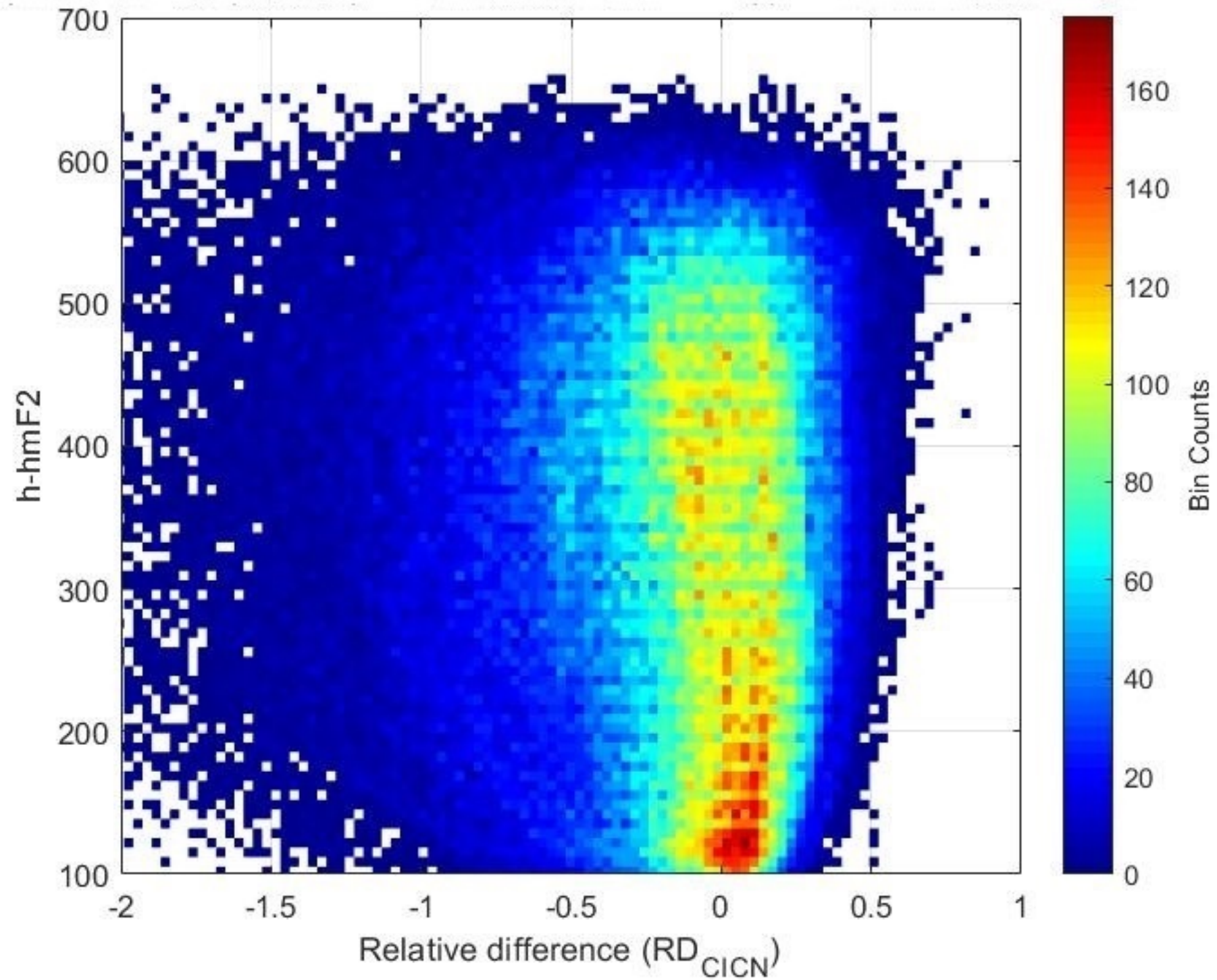
NRMSE for Matched Peak Profile



(b)

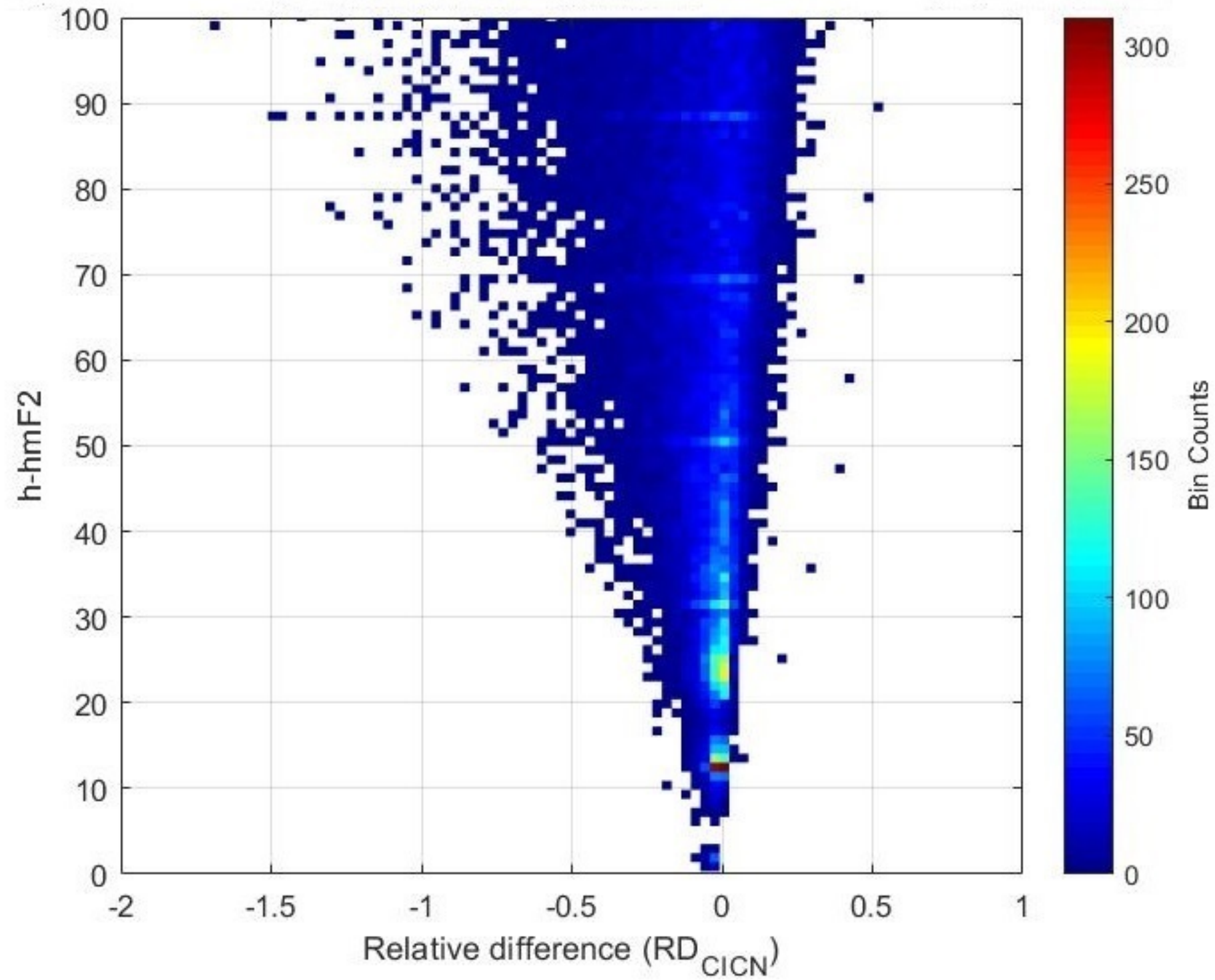
Figure 12.

COSMIC New<sub>g</sub> Corrected NeQuick matched peak profiles (h-hmF2>100)



(a)

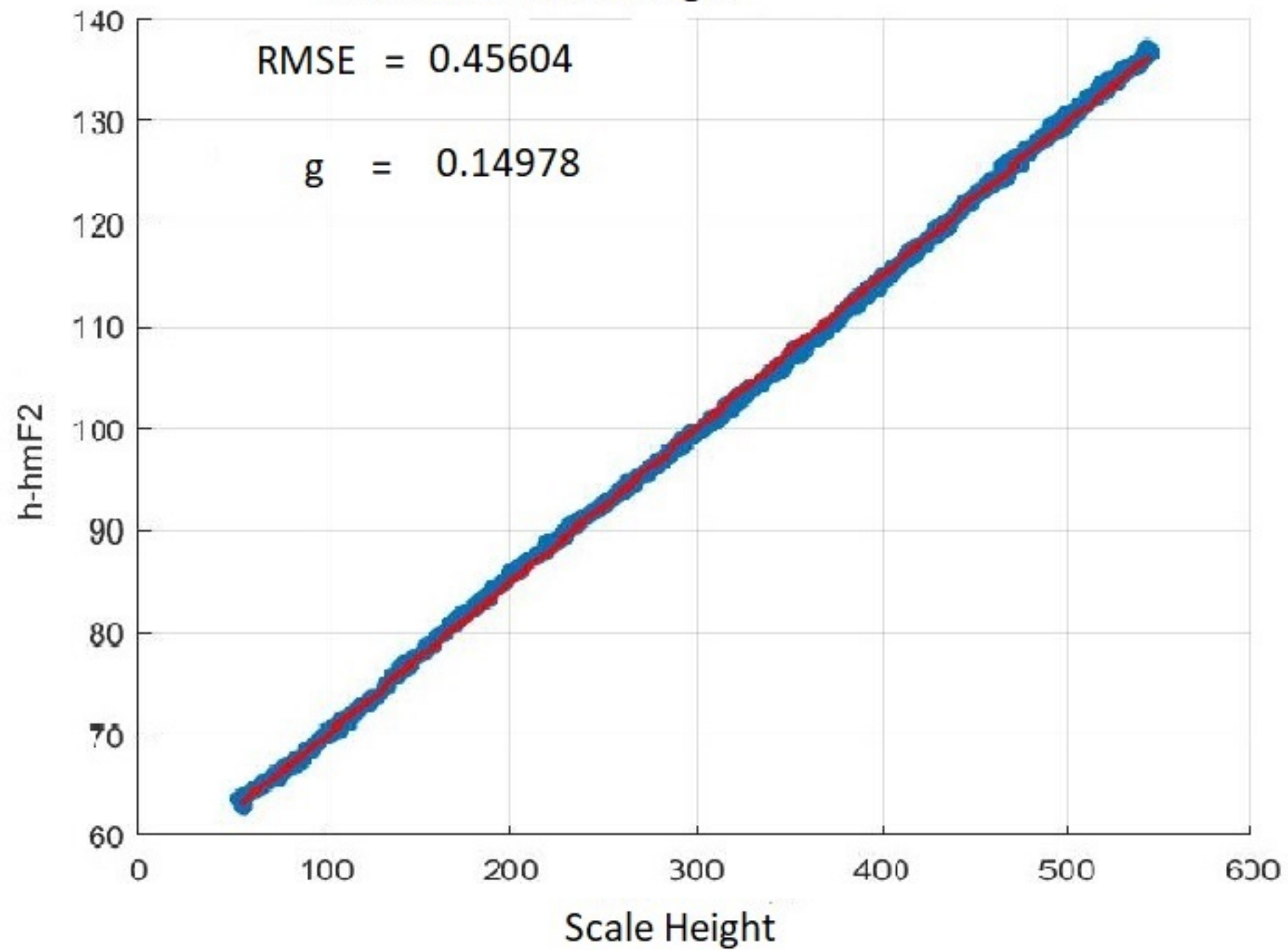
COSMIC New<sub>g</sub> Corrected NeQuick matched peak profiles (h-hmF2<100)



(b)

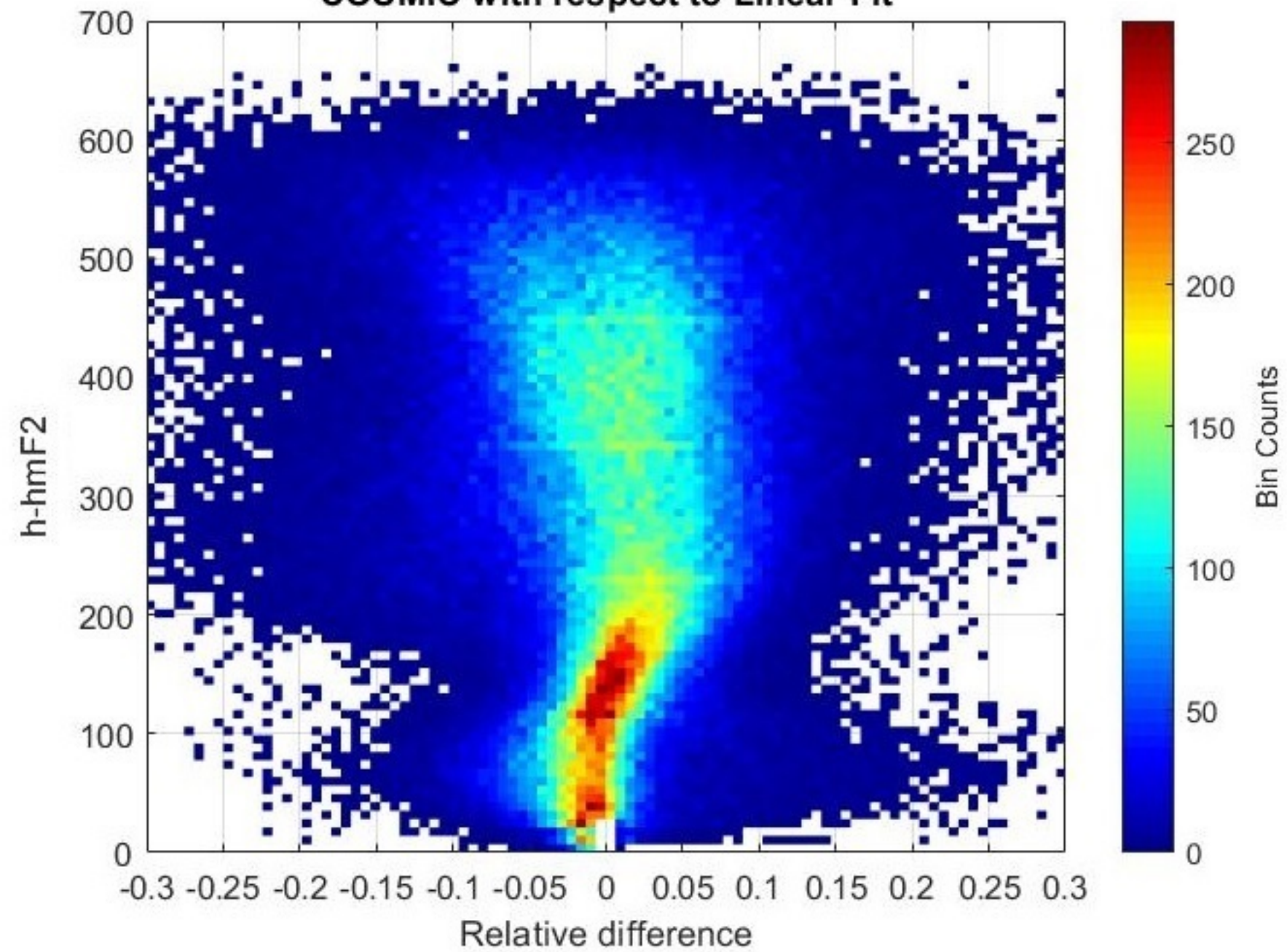
Figure 13.

Linear fit to Scale height



(a)

COSMIC with respect to Linear Fit



(b)

Figure 14.

g with respect to RMSE

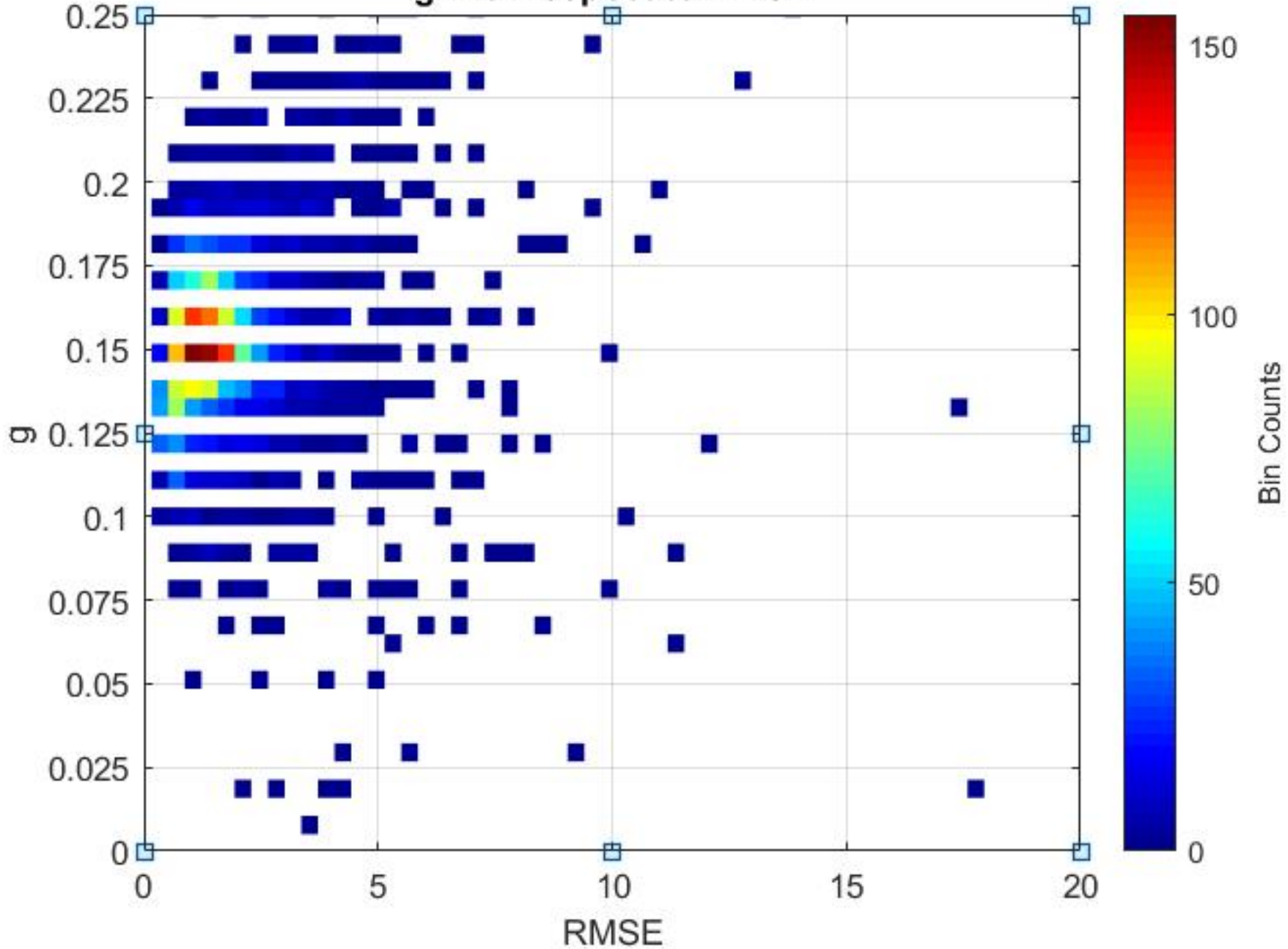


**Table 1**

<b>Station name (Country)</b>	<b>Geog. Lat. (°)</b>	<b>Geog. Lon. (°)</b>	<b>Geo Mag. Lat.(°)</b>	<b>Number of Coincident observations</b>	<b>Number of Matched Peak Profiles</b>
<b>Alpena (Michigan)</b>	45.07	-83.56	46.94	93	8
<b>Arenosillo (Spain)</b>	37.1	-6.7	30.82	701	55
<b>Arguello (USA)</b>	34.8	-120.5	40.31	429	28
<b>Ascension Island (UK)</b>	-7.95	-14.4	-18.28	542	49
<b>Athens (Greece)</b>	38	23.5	31.98	997	75
<b>Austin (USA)</b>	30.4	-97.7	32.60	238	55
<b>Boa (Brazil)</b>	2.88	60.7	5.62	46	2
<b>Boulder (USA)</b>	40	-105.3	48.35	1057	126
<b>Dourbes (Belgium)</b>	50.1	4.6	45.90	1637	249
<b>Eielson (Alaska)</b>	64.6	-147.7	65.65	224	33
<b>Fortaleza (Brazil)</b>	-3.9	-38.4	-6.41	234	14
<b>Gakona (USA)</b>	62.4	-145	62.99	1246	101
<b>Goose Bay (Canada)</b>	62.38	-145	60.46	229	30
<b>Grahamstown (South Africa)</b>	-33.3	26.5	-41.38	950	96
<b>Guam</b>	13.6	144.86	16.13	85	14

<b>Hermanus (South Africa)</b>	-34.42	19.22	30.99	885	164
<b>ICheon (South Korea)</b>	37.14	127.54	39.20	478	60
<b>Idaho (USA)</b>	43.81	-112.67	45.71	379	59
<b>Jeju (South Korea)</b>	33.43	126.3	26.81	562	83
<b>Jicamarca (Peru)</b>	-12	-76.8	0.09	283	12
<b>Juliusruh (Germany)</b>	54.6	13.4	50.71	1141	163
<b>Kwajalein (Marshall isl.)</b>	9	167.2	3.85	235	16
<b>Learmonth (Australia)</b>	-21.8	114.1	-32.25	607	65
<b>Louisvale (South Africa)</b>	-28.5	21.2	-37.67	688	100
<b>Madimbo (South Africa)</b>	-22.39	30.88	-32.33	1668	224
<b>Millstone Hill (USA)</b>	43.6	-71.5	51.77	1637	186
<b>Moscow (Russia)</b>	55.5	37.3	51.34	614	102
<b>Nicosia (Cyprus)</b>	35.14	33.2	29.23	468	27
<b>Nord (Greenland)</b>	81.4	-17.5		43	1
<b>Pruhonic (Czech Republic)</b>	50	14.6	45.49	1230	288
<b>Ramey (Puerto Rico)</b>	18.5	-67.1	27.59	390	57
<b>Rome</b>	41.9	12.5	36.03	858	108

<b>(Italy)</b>					
<b>Roquetes (Spain)</b>	40.8	0.5	34.98	1307	160
<b>King Salmon (USA)</b>	58.4	-156.4	56.89	795	87
<b>Sanya (China)</b>	18.34	109.42	20.78	124	3
<b>Sao Luis (Brazil)</b>	-2.6	-44.2	-2.27	203	12
<b>Sondrestrom (Greenland)</b>	66.98	-50.94	72.28	610	46
<b>Port Stanley (Falkland isl.)</b>	-51.6	-57.9	-38.88	1376	155
<b>Thule (Greenland)</b>	76.54	-68.44	76.05	143	11
<b>Tromso (Norway)</b>	69.58	19.22	66.52	897	135
<b>San Vito (Italy)</b>	40.6	17.8	34.73	758	104
<b>Wallops Island (USA)</b>	37.94	-75.58	47.83	1318	09
<b>Wuhan (China)</b>	30.5	114.4	32.70	75	10
<b>Yakutsk (Russia)</b>	62	129.6	56.33	583	51
<b>Total</b>				<b>29,063</b>	<b>3433</b>